Acta Mech 233, 233–257 (2022)
https://doi.org/10.1007/s00707-021-03112-3

ORIGINAL PAPER

Y. Zhang · J. Cai · C. Mi · F. Wang · A. H. Akbarzadeh

Effect of surface residual stress and surface layer stiffness on mechanical properties of nanowires

Received: 8 July 2021 / Revised: 24 October 2021 / Accepted: 9 November 2021 / Published online: 3 January 2022

Abstract The mechanical properties of nanowires are significantly affected by surface effects. In this work, we investigate the potential mechanisms of surface residual stress and surface layer stiffness on the bending behavior of nanowires. The deflection equation of nanowires under pure bending is first derived from the Young–Laplace equation and the Euler–Bernoulli beam theory. Subsequently, a new finite element model based on Galerkin's weighted residual method is developed to verify the accuracy of the theoretical solution. The theoretical and numerical solutions present the significant effects of surface residual stress and surface layer stiffness on the elastic properties of nanowires depending on the feature size, boundary conditions, and sectional geometry of the nanowires. Specifically, the surface residual stress makes the simply-supported and fixed–fixed nanobeams stiffer; however, it makes the cantilever nanobeam softer. Besides, the sectional geometry of the nanowires has a noticeable impact on their transverse deflection. If the size of circumscribed circle of the cross section remains constant, the nanowires become harder as the numbers of sectional sides increase for the specific feature size and boundary conditions. If the cross-sectional area remains unchanged, the deflection of the nanowires fluctuates as the number of cross-sectional side increases. We realize that the overall Young's modulus of nanowires is closely related to the feature size. As the cross-sectional feature size is below a critical value, the surface residual stress dominates the bending behavior of the nanowire. As the sectional feature size exceeds the critical feature size that is correlated to the nanowire boundary conditions, the factor dominating the bending behavior gradually transforms from the surface residual stress to the surface layer stiffness. This study provides a theoretical framework for developing a design strategy that incorporates surface effects in the engineering of nano/microscale architected advanced materials.

1 Introduction

Metamaterials [1–3] are artificial materials with unique structural designs to manipulate and control light [4], sound [5], mechanical stress [6], etc., leading to previously inaccessible properties in photonics [7], acoustics [5], deployability [8], reusable energy absorption [9], and many other multiphysical aspects

Y. Zhang · C. Mi (✉)
Jiangsu Key Laboratory of Engineering Mechanics, School of Civil Engineering, Southeast University, Nanjing 210096, Jiangsu, China
e-mail: mi@seu.edu.cn

J. Cai · A. H. Akbarzadeh (✉)
Department of Bioresource Engineering, McGill University, Montreal, QC H9X 3V9, Canada
e-mail: hamid.akbarzadeh@mcgill.ca

F. Wang
College of Civil Science and Engineering, Yangzhou University, Yangzhou 225127, China

A. H. Akbarzadeh
Department of Mechanical Engineering, McGill University, Montreal, QC H3A 0C3, Canada

[10, 11]. As an essential component of micro-/nanodevices, nanowires have a wide range of application in nanotechnology, micro-/nanoelectromechanical systems (M/NEMS), optoelectronics, and biotechnology [12–14]. Specifically, lightweight open-cell nanoscale cellular solids or recently developed nanoarchitected metamaterials with unprecedented multifunctional properties consisting of a rationally designed arrangement of struts can be regarded as composite structures comprised of interconnected nanowires with complex three-dimensional (3D) architecture [15–20]. The physical properties of these nanoarchitected metamaterials benefit from their unique architectural structure. The nonlinear mechanical responses can be tailored by the design of metamaterial unit-cell geometry. It has been shown experimentally that essentially any nonlinear mechanical behavior can be achieved, and even multistable behavior is achievable (buckling unit cell [21] in Fig. 1b) by a rational design of the underlying architecture of the building blocks of metamaterials [22–24]. Truss-based lattices with sizeable nodal connectivity turn out to be favorable for achieving considerable strength (octet-truss unit cell [21] in Fig. 1b). 3D microlattices approaching the maximum possible theoretical strength have also been introduced [25–27], and their mechanical performance in metastructures has been explored [28]. 3D auxetic materials with highly ordered packing were first observed in the deformation of metallic crystals [29]. A chiral mechanical metamaterial unit cell breaks not only space-inversion symmetry but also time-inversion symmetry [21]. This leads to an asymmetric cross-coupling between torques and displacements on the one hand and between forces and rotations on the other hand [21]. Analogous to the classical Gibson–Ashby theory [30], nanoarchitected metamaterials can be modeled as a three-dimensional network of nanowires, with alternative boundary conditions, consisting of a periodic and infinitely extending array of identical unit cells.

Because of the high surface area-to-volume ratio in nanoscale materials, atoms near the surface of a solid experience different local conditions compared to those away from the surface [31–33]. For example, due to the lack of compensation of the bond energy, the surface atoms of nanoscale foam metamaterials have additional potential energy relative to the internal atoms. This additional uncompensated bond energy makes the nanomaterials have some characteristics different from those of macromaterials. This interesting phenomenon is called the surface effect [34, 35]. Similar mechanisms are often captured in natural liquid-related media, e.g., the surface tension produced by the upward uncompensated hydrogen bond of water molecules on the air-water interface pushes the water strider to stay above the water surface for a long time [36]. Dewdrops on a summer morning appear as static droplets supported by many fine villi on the surface of the lotus leaf [37, 38]. All of these phenomena are due to the surface effect.

In mechanics, the well-known “smaller is stronger” phenomenon has been verified in most materials [39–42]. The mechanical strength of classical materials depends on the characteristic intrinsic size, i.e., the length scale characterizing the size and distribution of its flaws. As the characteristic size of the material is further reduced to the nanoscale, the effect of internal defects on the mechanical strength of the material is also reduced, e.g., single-crystalline nanowires can be considered as perfect crystals without defects in specific cases. Furthermore, quite a few studies have shown that when the characteristic size is below 100 nm, the surface effects will affect the mechanical properties of the structure, and this effect will be further enhanced as the characteristic size decreases [43]. Thus, with the change of structural characteristic size from macro- to micro-scale, the main factor influencing the strength size dependence of a material shifts from the number of internal defects to the surface effect. In quantifying the mechanical performance of materials, the specific stiffness is as important as the specific strength. Structural stiffness depends on the material category, architecture, relative density, etc., and often, high strength generally achieves high stiffness. Nevertheless, compared with strength, reducing the characteristic size of macroscale materials has not been shown to lead to any size dependence [44–46]. Taking advantage of stiffness size dependence in materials requires a further decrease in the characteristic size to the nanoscale [23].

As the most general nanoscale structure, nanowires are also significantly affected by the surface effect on specific mechanical properties, such as strength and stiffness [47], which have been more than once experimentally shown to be size-dependent [48–53]. Inspired by the capillary phenomenon of liquids, Gurtin et al. [54, 55] developed a mathematical framework to study the mechanical behavior of the nanoscale material surface. Over the last decades, Gurtin’s theory has been widely employed to reveal the size-dependent mechanical properties of nanoscale materials. Specifically, Gurtin regarded the surface of a nanomaterial as a zero-thickness film covering the bulk material that can only be stretched but not bend. The surface effect is considered to consist of two components that are dependent on the surface strain and independent of the surface strain. Here, the term dependent on the surface strain can be represented by the surface Young’s modulus, while the term independent of the surface strain is represented by the surface residual stress. This idea is described in detail in many papers, in both molecular dynamics simulations and nanoindentation tests [56, 57]. However, molecular dynamics proved the existence of a thin film with a specific thickness on the surface of nanomaterials that can

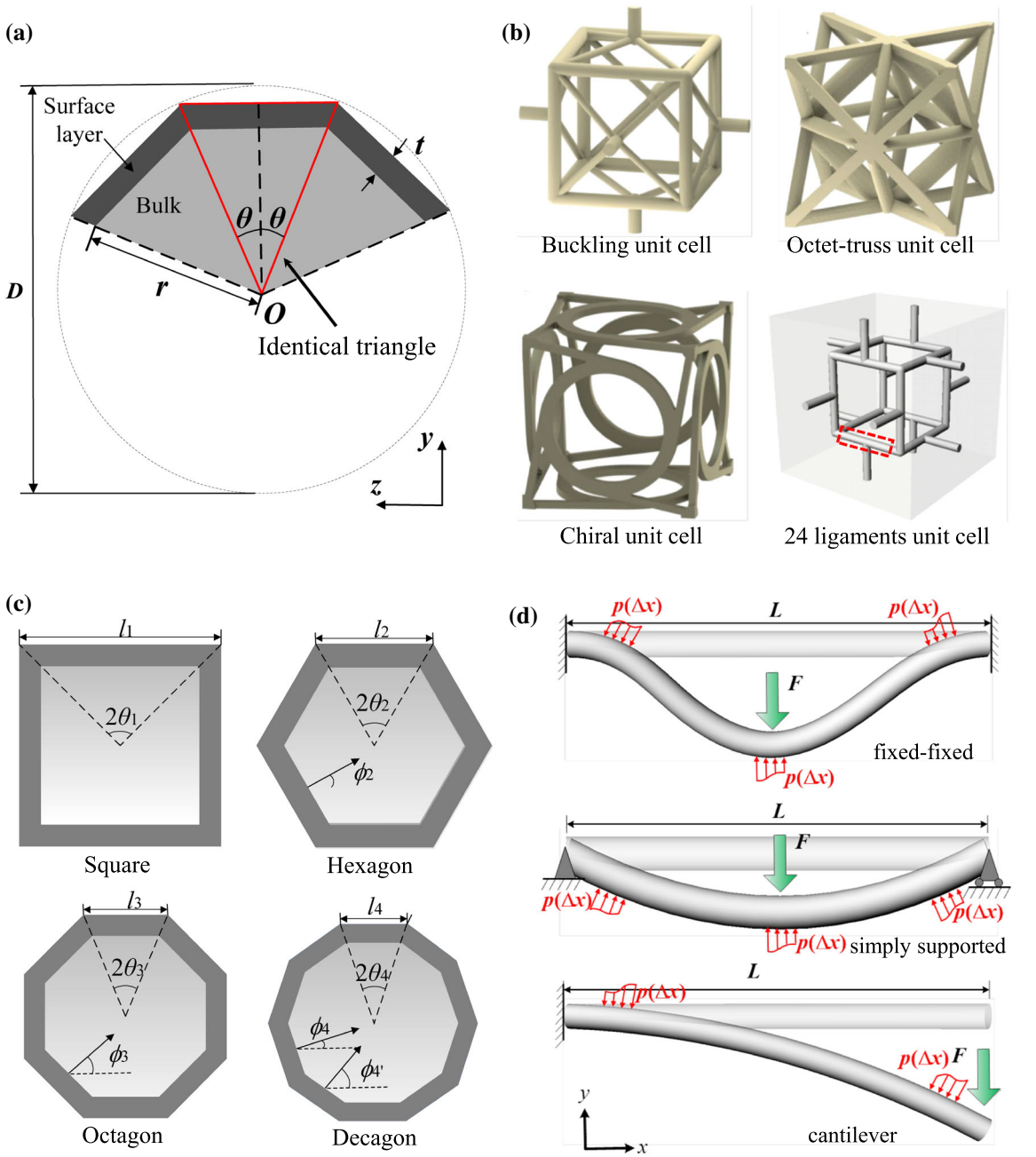

Fig. 1 Schematic figure of: **a** cross section of nanowires in the form of convex polygons, **b** four typical 3D unit cells made out of nanowires [21, 63], **c** four typical cross sections of nanowires, and **d** three typical boundary conditions of nanowires

withstand a certain bending moment, although this thin film is much smaller in size than the bulk materials [58, 59].

Due to neglecting the thickness of the surface layer, Gurtin's initial model applied to nanowires and porous foam materials is vividly called the core-surface model. A recently developed core–shell model, corresponding to the core-surface model and considering the thickness of the surface layer, is utilized to address the gap of missing bending resistance [60]. In recent years, the new core-shell model has dramatically expanded the development of theoretical nanomechanics, e.g., the bending deformation of nanowires and the effective Young's modulus of open-cell nanoscale cellular materials could be accurately predicted and evaluated by loading the surface parameters extracted from the nanoindentation experiments [61–64]. He et al. [61] incorporated the

surface effect from surface residual stress and surface elasticity in the elastic behavior of nanowires in static bending into the Euler-Bernoulli beam theory via the Young–Laplace equation. The solutions indicated that the cantilever nanowires behave as softer materials when deflected. The other structures, e.g., simply supported and fixed-fixed nanowires, become stiffer than original structures. Feng et al. [63] presented a unit-cell micromechanics model to predict the effective Young's modulus of open-cell nanoporous materials. The surface elastic theory was adopted to incorporate surface energy and surface residual stress on the effective elastic property of nanoporous materials. Xia et al. [65] used the theory of surface elasticity and the Timoshenko beam to investigate the surface effect on the mechanical behavior of nanoporous materials. Theoretical results showed that the effective Young's modulus of the nanoporous materials increases as the diameter of the strut decreases, but in contrast, the brittle collapse strength decreases with the diameter of the strut.

In addition to theoretical methods, computer simulation can also be employed to capture the mechanical response of nanoscale materials to some extent, e.g., the molecular dynamics method (MDM) and the finite element method (FEM). The molecular dynamics method based on real potential functions can simulate molecular trajectories of motion and the evolution of nanoscale materials under a series of multiphysical loads/stimuli [66, 67]. However, the inevitable cost of computer memory makes many researchers hesitate to intervene in structures with characteristic size above a few nanometers. Accordingly, FEM as an alternative method has widely been considered due to its simplicity, programmability, and affordable computational time. After more than half a century of development, the finite element method has evolved into a particularly powerful and versatile analysis technique and spread throughout multiple fields, especially after the release of several commercial finite element software packages [68–71]. Unfortunately, the existing finite element software packages are limited to assess the mechanical properties of macrostructures and suffer from the inability for modeling phenomena (e.g., size dependency and surface effects) occurring in nanoscale materials. For example, currently popular finite element packages such as ABAQUS and ANSYS include a rich library of cells that can simulate arbitrary geometries. They include libraries of various types of material models to simulate the properties of typical engineering materials, including metals, rubber, polymers, composites, reinforced concrete, compressible hyperelastic foams, soil, rock, and other geological materials. Despite the power of these finite element packages, they still cannot include element and material libraries for nanomaterials in initial programs. This is due to the fact that the complex surface/interface effects in nanomaterials are influenced by many factors, even the molecular arrangement of the material, making it impossible to develop a complete and convincing system of finite element theory in the field of nanomaterials at the current stage. Conversely, theoretical approaches based on the Gurtin-Murdoch and Steigmann-Ogden surface/interface models have now been implemented in numerous scenarios to describe the physical fields of nanomaterials. For example, Mi et al. [43, 72, 73] studied the stress concentration near circular holes in an elastic half-space and elastic infinite space. Nevertheless, unlike the finite element method, the current popular theoretical methods (e.g., the Gurtin–Murdoch method and Steigmann–Ogden method) capable of nanoscale effects can only be used for simple geometrical models, loading, and boundary conditions, due to the limitations of complex mathematical formulas for describing the mechanical performance of nanomaterials. Thus, the design of a finite element program applicable to the nanoscale will greatly expand the development of nano/multiscale advanced materials. Tian et al. [74] investigated the size-dependent deformations of two-dimensional nanosized structures with surface effects by the finite element method. He et al. [75] presented a computational method that can be applied to capture surface stress and surface tension-driven effects in nanostructures. Although the existing finite element programs established in the current literature are only effective in a small range, including some specific problems, the development of general finite element programs still encounters some insurmountable obstacles. For example, the numerical results of Wang and He do not correspond well to the theoretical solutions because the bending resistance of the surface layer of nanomaterials is ignored. Therefore, a more accurate and general finite element program must be developed to expand the application of finite element methods in the field of nanomechanics. Nanowires as the simplest form of nanostructures and the smallest unit of nano-architected metamaterials should be considered first.

Although surface effects have been proven to be one of the inherent properties of nanomaterials and have attracted widespread attention in the past few decades, there are still some ambiguous and even contradictory descriptions about the mechanism of the surface effect of nanostructures in the current widely cited literature. For example, Zheng et al. [76] and Feng et al. [63] thought that the surface layer stiffness is the most critical factor for the size effect of nanomaterials relative to the surface residual stress. However, Goudarzi et al. [77] and Moshtaghin et al. [78] obtained a size-dependent yield function for nanoporous materials by considering the residual surface stress and the surface elasticity. The results indicated that the surface residual stress is more important compared with the surface elasticity on the buckling strength and the yield strength. So far,

almost all relevant literature is devoted to describing the single factor. Still, there is a paucity of in-depth research on the internal relationship among the influencing factors of surface effects. As mentioned earlier, the enhancement and competition mechanism of surface residual stress and surface layer stiffness on the surface effect of nanomaterials is still unclear, and their intrinsic relationship should be studied in greater detail.

Besides that, all of the above efforts focused on the effect of residual stress, film stiffness, and boundary conditions on the mechanical behavior of nanowires. Nevertheless, the latest experimental measurements show that the mechanical properties of nanowires often exhibit a dependence on sectional geometry [79–81]. Zheng et al. [76] investigated the size-dependent elastic property of nanowires induced by the surface effect using the classical core-shell model. The effective Young's modulus of nanowires with regular polygonal cross sections was unified into a simple and explicit relation. Interestingly, to simplify the calculation model, the influence of surface residual stress was ignored in Zheng et al.'s [76] discussion. Thus, the influence mechanism of the sectional geometry on the bending deformation of nanowires should be reassessed considering the surface residual stress.

Therefore, the goal of this article is to employ theory and finite element methods to reveal the competitive mechanism of surface residual stress and surface layer stiffness on the surface effect of a nanowire structure in consideration of cross-sectional geometry and quantitatively explain the critical role of structural feature size in this process. The paper is organized as follows: Sect. 2 derives the deflection equation considering the sectional geometry of nanowires by the Young-Laplace equation and Euler-Bernoulli beam theory and develops a new finite element model based on Galerkin's weighted residual method to verify the accuracy of the theoretical solution. The role of surface layer stiffness on the effective Young's modulus is presented in Sect. 3.1. Section 3.2 introduces the influence of surface residual stress on the bending deformation and overall Young's modulus of nanowires under consideration of different boundary conditions. The influence of sectional geometry and the competitive mechanism of surface residual stress and surface layer stiffness on mechanical properties of nanowires is discussed in Sects. 3.3 and 3.4 to provides design guidelines for developing micro/nano-devices and nanoarchitected metamaterials. Section 4 highlights the principal conclusions extracted from the present research.

2 Governing equations

2.1 Derivation of effective bending stiffness

A nanowire with modified surface layers can be treated as a composite wire with a core–shell structure composed of a core having a modulus of bulk material and a surface shell coaxial with the core but having a surface modulus which is correlated with the surface bond length contractions [60]. This hypothetical model is similar to a functional coating composite material with a certain coating thickness, but the surface effect extending deep into the bulk is a gradual process and fades off slowly for the real surface layer of the nanowire. To simplify the problem and without influencing the analysis of the problem, we still treat the relaxed surface layers approximately as a uniform shell possessing an average bond contraction through the overall thickness. In this paper, to represent the most general form of nanowire cross section, a core-shell model [60] with an n-regular polygonal cross section is employed. Distinguishing from the core-surface model, as mentioned above, the bulk component is covered with a thin surface layer of thickness t, with a Young's modulus distinct from the bulk value in the employed core-shell model. The elastic property of the surface layer is usually anisotropic and depends on crystal orientation, surface roughness, and defects [76]. Also, for simplification, the isotropy assumption is used for both surface layer and bulk component. Figure 1a shows the most general cross-sectional diagrams of nanowires with n-regular polygons in a Cartesian coordinate system and a Polar coordinate system.

As seen in Fig. 1a, the n-regular polygon is divided into n completely identical triangles. Thus, the polar moment of inertia with respect to O of each identical triangle can be expressed as

$$I'_O = \iint_A \left(y^2 + z^2\right) \mathrm{d}y\mathrm{d}z = \frac{D^4}{32}\left(\frac{1}{3}\sin^3\theta\cos\theta + \sin\theta\cos^3\theta\right), \tag{1}$$

where A is the area of each identical triangle, D is the diameter of circumscribed circle of the regular polygon, and θ is half of the center angle of each identical triangle, respectively. Usually, the smallest dimension of the structure is also called the feature size; so here we define the circumscribed circle diameter D as the feature size of the nanobeam. The polar moment of inertia concerning O of the complete regular polygon is determined

by $I_o = nI_o'$ and n is the edge number of the polygon. According to the symmetry of regular polygon, the area moment of inertia with respect to the y-axis is expressed as $I_y = \frac{1}{2} I_o$.

The effective bending stiffness of nanowire is determined by [60, 61, 63]

$$E_e I_e = E_b I_b + E_s I_s, \tag{2}$$

where E_e, E_b, and E_s represent Young's modulus of effective entirety, bulk, and the surface layer and I_e, I_b, and I_s denote moment of inertia of area with respect to the x-axis for effective entirety, bulk, and the surface layer, respectively. According to geometry relations in Fig. 1a, the following equations can be derived:

$$\begin{aligned} r =& \frac{D}{2} - t\sec\theta,\ I_e = I_y = \frac{nD^4}{64}\left(\frac{1}{3}\sin^3\theta\cos\theta + \sin\theta\cos^3\theta\right), \\ I_b =& \frac{n}{64}(2r)^4\left(\frac{1}{3}\sin^3\theta\cos\theta + \sin\theta\cos^3\theta\right), \\ I_s =& I_e - I_b = \frac{n}{64}\left[D^4 - (2r)^4\right]\left(\frac{1}{3}\sin^3\theta\cos\theta + \sin\theta\cos^3\theta\right), \end{aligned} \tag{3}$$

where r is the circumscribed circle radius of the n-regular polygon of the core in Fig. 1a. Substituting Eq. (3) into (2), the effective bending stiffness of nanowire is derived as:

$$E_e I_e = \frac{n}{64}\left(\frac{1}{3}\sin^3\theta\cos\theta + \sin\theta\cos^3\theta\right)\left\{E_b(D-2t)^4 + E_s\left[D^4 - (D-2t)^4\right]\right\}. \tag{4}$$

The above-mentioned derivation provides a relationship between the effective bending stiffness of nanowire and the Young's modulus of their components. Equation (4) clearly shows the size-dependent effective Young's modulus as a function of the thickness of the surface layer. Some details will be described in Sect. 3.1.

2.2 Bending deflection of nanowires

According to Gurtin et al.'s theory [54, 55], the constitutive relation of the surface layer can be expressed as [61, 63]

$$\sigma_{ij} = \sigma_{ij}^0 + C_{ijkl}\varepsilon_{kl}, \tag{5}$$

where σ_{ij} is surface stress tensor, ε_{kl} is surface strain tensor, C_{ijkl} represents surface stiffness tensor, and $\sigma 0$ ij is residual surface stress tensor, respectively. For nanowires, Eq. (5) is simplified to [61, 63]

$$\tau = \tau_0 + E_0\varepsilon, \tag{6}$$

in which τ is the surface stress parallel to the material surface, ε is the surface strain, $E_0 = E_s t$ is the effective surface Young's modulus, and τ_0 is the residual surface stress, respectively. Therefore, the surface stress is described as the summation of two terms; one is a *strain-independent term* and the other is a *strain-dependent term*.

A transverse distributed force along the nanowire longitudinal direction is generated from the surface stress in bending as described by the Young–Laplace equation [47, 61, 63, 82, 83]. Under small deformation assumption, the transverse distributed force can be expressed as [84]

$$p(x) = Hw''(x), \tag{7}$$

where w is the transverse deflection of the nanowire, prime stands for the derivative concerning the coordinate x, and H is an intermediate parameter which is determined by the cross-sectional shape of nanowire and surface stress along the longitudinal direction nanowire.

Figure 1c shows the schematic figure of nanowires with the cross-sectional shapes of square, regular hexagon, regular octagon, and regular decagon, respectively. We assume that the plane of transverse deflection is perpendicular to the z-axis. Thus, the transverse distributed force of nanowires can be expressed as:

$$\begin{aligned} p_1(x) &= 2\tau l_1 w''(x) = 2\tau D\cos\theta_1 w''(x), \\ p_2(x) &= 2(\tau\sin\phi_2 l_2 + \tau l_2 + \tau\sin\phi_2 l_2)w''(x) = 2\tau D w''(x), \end{aligned}$$

$$p_3(x) = 2(\tau \sin\phi_3 l_3 + \tau l_3 + \tau \sin\phi_3 l_3)w''(x) = 2\tau D\cos\theta_3 w''(x),$$
$$p_4(x) = 2(\tau \sin\phi_4 l_4 + \tau \sin\phi_4 l_4 + \tau l_4 + \tau \sin\phi_{4'} l_4 + \tau \sin\phi_{4'} l_4)w''(x) = 2\tau D w''(x), \quad (8)$$

in which $p_1(x)$, $p_2(x)$, $p_3(x)$, and $p_4(x)$ are the associated transverse distributed forces of nanowires with the cross-sectional shape of square, regular hexagon, regular octagon, and regular decagon, respectively. Please refer to Fig. 1c for the other parameters used in Eq. (8). We can further simplify Eq. (8) in the form of Eq. (7) as:

$$p(x) = Hw''(x), \quad \text{where} \quad H = \begin{cases} 2\tau D\cos\theta, & (n = 4a), \\ 2\tau D, & (n = 4a+2), \end{cases} \quad (9)$$

where a denotes a positive integer greater than zero. Based on the small deformation assumption, the longitudinal strain of nanowires can be expressed by

$$\varepsilon = \pm y_0 w''(x) \quad (10)$$

in which y_0 is the distance from the side surface of the nanowire to the neutral axis z. Substituting Eqs. (6) and (10) into Eq. (9) yields

$$p(x) = Hw''(x) = \begin{cases} 2\{\tau_0 + E_0[\pm y_0 w''(x)]\} D\cos\theta w''(x), & (n = 4a), \\ 2\{\tau_0 + E_0[\pm y_0 w''(x)]\} D w''(x), & (n = 4a+2), \end{cases} \quad (11)$$

Neglecting the square of the second derivative of deflection, $p(x)$ is determined by

$$p(x) = H_0 w''(x), \quad H_0 = \begin{cases} 2\tau_0 D\cos\theta, & (n = 4a), \\ 2\tau_0 D, & (n = 4a+2). \end{cases} \quad (12)$$

It is necessary to note that when n tends to infinity, the cross-sectional shape of nanowire gradually evolves into a circle, and the value of H_0 is unified into $2\tau_0 D$. Based on the small deformation assumption, the curvature of a nanowire can be expressed as

$$w''(x) = \frac{M}{E_e I_e}, \quad (13)$$

where M is the bending moment loading on the nanowire. The transverse distributed force of nanowires can also be expressed as

$$p(x) = \frac{\mathrm{d}^2 M}{\mathrm{d}x^2}. \quad (14)$$

Substituting Eq. (13) into (14), the transverse distributed force of nanowires can be derived as

$$p(x) = E_e I_e w''''(x). \quad (15)$$

Equation (15) is a standard fourth-order linear constant coefficient homogeneous differential equation. The solution of Eq. (15) can be expressed as

$$w(x) = C_1 + C_2 x + C_3 e^{\sqrt{\lambda}x} + C_4 e^{-\sqrt{\lambda}x},$$
$$\lambda = \frac{H_0}{E_e I_e}, \quad (16)$$

where C_1, C_2, C_3, and C_4 are constant coefficients.

Most microstructures of open-cell nanofoam structures can be regarded as the specific arrangement of nanowires with different boundary conditions [63]. Figure 1d shows the diagram of bending nanowires with different boundary conditions: cantilever, simply supported beam, and fixed–fixed beam. L is the initial length of the nanowire. To generate the initial curvature on nanowires, a constant concentrated force F is applied at $x = L$ for cantilever nanowire and $x = L/2$ for simply supported beam and fixed-fixed beam. By enlarging a specific beam in the 24 ligaments unit cell in Fig. 1b, the same fixed-fixed boundary conditions with Fig. 1d can be obtained. It should be noted that for exploring new materials, the human's goal is always to seek

a more stable structural form that can be periodically arranged in space. Therefore, relatively stable fixed-fixed beams or trusses are the most basic structures in open-cell nanofoam materials, while simply supported and cantilevered ones are exceedingly rare. Nevertheless, simply supported and cantilevered beams are still assessed for comparison.

According to nanowires' loading and deformation features, boundary conditions can be divided into the following three groups

$$\begin{cases} w(0) = 0, \\ w'(0) = 0, \\ Q(0) = F + \int_0^L p(x)\mathrm{d}x = -E_e I_e w'''(0), \\ M(0) = FL + \int_0^L p(x)x\mathrm{d}x = E_e I_e w''(0); \end{cases} \quad \text{(cantilever)} \tag{17a}$$

$$\begin{cases} w(0) = 0, \\ w'\left(\frac{L}{2}\right) = 0, \\ w''(0) = 0, \\ Q(0) = \frac{F}{2} + \int_0^{\frac{L}{2}} p(x)\mathrm{d}x = -E_e I_e w'''(0); \end{cases} \quad \text{(simply supported beam)} \tag{17b}$$

$$\begin{cases} w(0) = 0, \\ w'(0) = 0, \\ w'\left(\frac{L}{2}\right) = 0, \\ Q(0) = \frac{F}{2} + \int_0^{\frac{L}{2}} p(x)\mathrm{d}x = -E_e I_e w'''(0). \end{cases} \quad \text{(fixed - fixed beam)} \tag{17c}$$

Substituting Eqs. (15) and (16) into Eqs. (17a)–(17c), the transverse deflection can be derived as

$$\begin{cases} w(x) = \frac{-F}{2E_e I_e \lambda\sqrt{\lambda}}\left(e^{\sqrt{\lambda}L} - e^{-\sqrt{\lambda}L}\right) + \frac{F}{2E_e I_e \lambda}\left(e^{\sqrt{\lambda}L} + e^{-\sqrt{\lambda}L}\right)x + \frac{-F}{2E_e I_e \lambda\sqrt{\lambda}}e^{-\sqrt{\lambda}L}e^{\sqrt{\lambda}x} + \frac{F}{2E_e I_e \lambda\sqrt{\lambda}}e^{\sqrt{\lambda}L}e^{-\sqrt{\lambda}x}, \\ \quad x \in [0, L] \text{ (cantilever)} \\ w(x) = \frac{F}{2E_e I_e \lambda}x - \frac{F}{2E_e I_e \lambda\sqrt{\lambda}\left(e^{\sqrt{\lambda}\frac{L}{2}} + e^{-\sqrt{\lambda}\frac{L}{2}}\right)}e^{\sqrt{\lambda}x} + \frac{F}{2E_e I_e \lambda\sqrt{\lambda}\left(e^{\sqrt{\lambda}\frac{L}{2}} + e^{-\sqrt{\lambda}\frac{L}{2}}\right)}e^{-\sqrt{\lambda}x}, \\ \quad x \in \left[0, L/2\right] \text{ (simply supported beam)} \\ w(x) = \frac{F}{2E_e I_e \lambda\sqrt{\lambda}}\left(\frac{1-e^{\sqrt{\lambda}\frac{L}{2}}}{1+e^{\sqrt{\lambda}\frac{L}{2}}} + \sqrt{\lambda}x - \frac{e^{\sqrt{\lambda}x}}{1+e^{\sqrt{\lambda}\frac{L}{2}}} + \frac{e^{\sqrt{\lambda}\frac{L}{2} - \sqrt{\lambda}x}}{1+e^{\sqrt{\lambda}\frac{L}{2}}}\right), \\ \quad x \in \left[0, L/2\right] \text{ (fixed-fixed beam)} \end{cases} \tag{18}$$

When λ approaches zero, Eq. (18) can be simplified as a bending deflection equation of a beam in the classical case:

$$\begin{cases} w(x) = \frac{F(3L-x)x^2}{6E_e I_e}, \quad x \in [0, L] \text{ (cantilever)} \\ w(x) = \frac{F\left(3L^2-4x^2\right)x}{48E_e I_e}, \quad x \in \left[0, L/2\right] \text{ (simply supported beam)} \\ w(x) = \frac{F(3L-4x)x^2}{48E_e I_e}, \quad x \in \left[0, L/2\right] \text{ (fixed-fixed beam)} \end{cases} \tag{19}$$

2.3 Finite element formulation

In Sect. 2.2, an analytic solution of the nanowire deflection based on the Young–Laplace equation and Euler–Bernoulli beam theory is developed by strict formula derivation. In this section, a finite element based on Galerkin's weighted residual theory will be utilized to study the deformation of nanowires.

A differential equation with a simple boundary condition is considered as

$$L(w) = f, \quad x \in \Omega, \tag{20}$$

where w is a function of the dependent variable x, f is a known function independent of w, and Ω is the definition field of the independent variable x, respectively. The approximate solution of w can be expressed by a family of trial functions with specific coefficients

$$w \approx \overline{w} = \sum_{i=1}^{n} \alpha_i \varphi_i, \tag{21}$$

where α_i is the specific coefficient, φ_i is the trial function, and $\overline{w}$ is the approximate solution of w, respectively. Obviously, the approximate solution cannot satisfy the differential Eq. (20) accurately. Therefore, the residual generated by the approximate solution can be expressed as

$$R = L(\overline{w}) - f. \tag{22}$$

For the exact solution, any point in the definition field Ω can satisfy Eq. (20), and residual R is equal to zero. For the approximate solution, the weight function W_j $(j = 1, 2, \ldots, n)$ is introduced to make the weighted integral value of residual R equal to zero. Actually, this process is equivalent to constructing the inner product of the residual and the weight function and making it equal to zero. Substituting Eq. (22), the integral expression can be written as

$$\int_{\Omega} W_j R \mathrm{d}\Omega = \int_{\Omega} W_j [L(\overline{w}) - f] \mathrm{d}\Omega = 0, \quad (j = 1, 2, 3 \ldots n). \tag{23}$$

The basic idea of the weighted residual method is to find n weight functions to calculate n unknown coefficients to obtain approximate solutions of the differential equation. The larger the value of n is, the higher the accuracy of approximate solution of the differential equation will be.

Galerkin's weighted residual method is a simple form of the weighted residual method, which takes the trial function of the approximate solution as a weighted function. Thus, Eq. (23) can also be expressed as

$$\int_{\Omega} \varphi_j [L(\overline{w}) - f] \mathrm{d}\Omega = 0, \quad (j = 1, 2, 3 \ldots n). \tag{24}$$

When n tends to infinity, the approximate solution will converge to the exact solution. Substituting Eq. (21) into Eq. (24), the integral formula can be written as

$$\int_{\Omega} \varphi_j [L(w) - f] \mathrm{d}\Omega = 0, \quad (j = 1, 2, 3 \ldots n). \tag{25}$$

The first variation of Eq. (21) can be written as

$$\delta w = \sum_{i=1}^{n} \varphi_i \delta \alpha_i, \tag{26}$$

where δ is the sign of variational operation. Meanwhile, multiplying Eq. (25) by $\delta \alpha_j$ and summing them up gives

$$\int_{\Omega} [L(w) - f] \left(\sum_{j=1}^{n} \varphi_j \delta \alpha_j \right) \mathrm{d}\Omega = 0, \quad (j = 1, 2, 3 \ldots n). \tag{27}$$

Substituting Eq. (26) into Eq. (27), we obtain

$$\int_{\Omega} [L(w) - f] \delta w \mathrm{d}\Omega = 0. \tag{28}$$

Equation (28) is the variational form of Galerkin's formula. For mechanical problems, the mechanical meaning of Eq. (28) is equivalent to the principle of virtual work [85, 86]. For static loading of a beam, substituting Eq. (12) into Eq. (15) and adding external load $f(x)$, the deflection governing equation can be written as

$$E_e I_e \frac{\mathrm{d}^4 w}{\mathrm{d}x^4} - H_0 \frac{\mathrm{d}^2 w}{\mathrm{d}x^2} + f(x) = 0. \tag{29}$$

Galerkin's weighted residual method is applied to Eq. (29) to develop the finite element formulation. According to Eq. (28), the weighted residual statement of Eq. (29) can be expressed as

$$\int_0^L \left[E_e I_e \frac{\mathrm{d}^4 w}{\mathrm{d}x^4} - H_0 \frac{\mathrm{d}^2 w}{\mathrm{d}x^2} + f(x) \right] \delta w \mathrm{d}x = 0. \tag{30}$$

Integrating Eq. (29) by parts gives the weak formulation as

$$\int_0^L \left[E_e I_e \frac{\mathrm{d}^2 w}{\mathrm{d}x^2} \frac{\mathrm{d}^2 \delta w}{\mathrm{d}x^2} + H_0 \frac{\mathrm{d}w}{\mathrm{d}x} \frac{\mathrm{d}\delta w}{\mathrm{d}x} + f(x)\delta w \right] \mathrm{d}x + \left\{ -E_e I_e \frac{\mathrm{d}^2 w}{\mathrm{d}x^2} \frac{\mathrm{d}\delta w}{\mathrm{d}x} + \left[E_e I_e \frac{\mathrm{d}^3 w}{\mathrm{d}x^3} - H_0 \frac{\mathrm{d}w}{\mathrm{d}x} \right] \delta w \right\} \Big| \begin{matrix} L \\ 0 \end{matrix} = 0. \tag{31}$$

Because simply supported beam and fixed-fixed beam have fixed boundaries at the beginning and the end, the second term on the left of Eq. (31) can be ignored. Therefore, Eq. (31) can be simplified as

$$\int_0^L \left[E_e I_e \frac{\mathrm{d}^2 w}{\mathrm{d}x^2} \frac{\mathrm{d}^2 \delta w}{\mathrm{d}x^2} + H_0 \frac{\mathrm{d}w}{\mathrm{d}x} \frac{\mathrm{d}\delta w}{\mathrm{d}x} + f(x)\delta w \right] \mathrm{d}x = 0. \tag{32}$$

Divide the nanowire into n finite units, and thus, there are $n + 1$ nodes in the [0-L] interval as $x_0 = 0$, x_1, $x_2 \ldots x_{i-1}$, $x_i \ldots x_n = L$, respectively. Therefore, the subinterval of any element can be expressed as [$x_{i\text{-}1}$, x_i]. The integral formula of subunit can be expressed as

$$\phi = \int_{x_{i-1}}^{x_i} \left[E_e I_e \frac{\mathrm{d}^2 w}{\mathrm{d}x^2} \frac{\mathrm{d}^2 \delta w}{\mathrm{d}x^2} + H_0 \frac{\mathrm{d}w}{\mathrm{d}x} \frac{\mathrm{d}\delta w}{\mathrm{d}x} + f(x)\delta w \right] \mathrm{d}x. \tag{33}$$

We consider a two-node beam finite element with three degrees of freedom per node, i.e., u, w, and $\theta = \mathrm{d}w/\mathrm{d}x$. The element nodal displacement vector is

$$\mathbf{U}_e = \left[u_1 w_1 \theta_1 u_2 w_2 \theta_2 \right]^{\mathrm{T}}. \tag{34}$$

The displacement is interpolated considering a linear displacement pattern in u-direction and a triple displacement pattern in v-direction as

$$\mathbf{u} = \begin{bmatrix} u \\ w \end{bmatrix} = \mathbf{N}(x)\mathbf{U}_e, \tag{35}$$

where $\mathbf{N}(x)$ is the shape function matrix with the elements

$$\mathbf{N}(x) = \begin{bmatrix} N_1 & 0 & 0 & N_4 & 0 & 0 \\ 0 & N_2 & N_3 & 0 & N_5 & N_6 \end{bmatrix}, \tag{36}$$

$$N_1 = 1 - \frac{x}{l},\ N_2 = 1 - \frac{3}{l^2}x^2 + \frac{2}{l^3}x^3,\ N_3 = -x + \frac{2}{l}x^2 - \frac{1}{l^2}x^3,$$
$$N_4 = \frac{x}{l},\ N_5 = \frac{3}{l^2}x^2 - \frac{2}{l^3}x^3,\ N_6 = \frac{1}{l}x^2 - \frac{1}{l^2}x^3, \tag{37}$$

where l is the length of the element. Dividing shape function matrix $\mathbf{N}(x)$ into two sections, i.e., $\mathbf{N}_u(x)$ and $\mathbf{N}_w(x)$, and thus $\mathbf{N}(x)$ can be written as

$$\mathbf{N}(x) = \begin{bmatrix} \mathbf{N}_u(x) \\ 0 \end{bmatrix} + \begin{bmatrix} 0 \\ \mathbf{N}_w(x) \end{bmatrix}, \tag{38}$$

$$\mathbf{N}_u(x) = \begin{bmatrix} N_1 & 0 & 0 & N_4 & 0 & 0 \end{bmatrix},$$
$$\mathbf{N}_w(x) = \begin{bmatrix} 0 & N_2 & N_3 & 0 & N_5 & N_6 \end{bmatrix}, \tag{39}$$

where $\mathbf{N}_u$(x) and $\mathbf{N}_w$(x) are shape function matrix related to longitudinal displacement u and transverse deflection w. Therefore, Eq. (35) can be divided as

$$u = \mathbf{N}_u(x)\mathbf{U}_e,$$
$$w = \mathbf{N}_w(x)\mathbf{U}_e. \tag{40}$$

The first variation of the second term of Eq. (40) is

$$\delta w = \mathbf{N}_w(x)\delta\mathbf{U}_e. \tag{41}$$

Substituting Eq. (41) into Eq. (33), the Galerkin's equation of element can be obtained

$$\begin{aligned}\phi &= \delta\mathbf{U}_e^T \int_{x_{i-1}}^{x_i} \left[E_e I_e \frac{\mathrm{d}^2\mathbf{N}_w^T}{\mathrm{d}x^2}\frac{\mathrm{d}^2\mathbf{N}_w}{\mathrm{d}x^2} + H_0 \frac{\mathrm{d}\mathbf{N}_w^T}{\mathrm{d}x}\frac{\mathrm{d}\mathbf{N}_w}{\mathrm{d}x}\right] dx\mathbf{U}_e + \delta\mathbf{U}_e^T \int_{x_{i-1}}^{x_i} f(x)\mathbf{N}_w^T \mathrm{d}x \\ &= \delta\mathbf{U}_e^T \mathbf{K}_w \mathbf{U}_e - \delta\mathbf{U}_e^T \mathbf{R}_w, \end{aligned} \tag{42}$$

$$\begin{aligned}\mathbf{K}_w &= \int_{x_{i-1}}^{x_i} \left[E_e I_e \frac{\mathrm{d}^2\mathbf{N}_w^T}{\mathrm{d}x^2}\frac{\mathrm{d}^2\mathbf{N}_w}{\mathrm{d}x^2} + H_0 \frac{\mathrm{d}\mathbf{N}_w^T}{\mathrm{d}x}\frac{\mathrm{d}\mathbf{N}_w}{\mathrm{d}x}\right] \mathrm{d}x, \\ \mathbf{R}_w &= -\int_{x_{i-1}}^{x_i} f(x)\mathbf{N}_w^T \mathrm{d}x, \end{aligned} \tag{43}$$

where $\mathbf{K}_w$ and $\mathbf{R}_w$ represent element stiffness matrix and element load only considering the deflection w. Substituting Eq. (37) and (39) into Eq. (43), element stiffness matrix $\mathbf{K}_w$ is then obtained as

$$\mathbf{K}_w = \begin{bmatrix} 0 & 0 & 0 & 0 & 0 & 0 \\ 0 & \frac{12E_eI_e}{l^3} & -\frac{6E_eI_e}{l^2} & 0 & -\frac{12E_eI_e}{l^3} & -\frac{6E_eI_e}{l^2} \\ 0 & -\frac{6E_eI_e}{l^2} & \frac{4E_eI_e}{l} & 0 & \frac{6E_eI_e}{l^2} & \frac{2E_eI_e}{l} \\ 0 & 0 & 0 & 0 & 0 & 0 \\ 0 & -\frac{12E_eI_e}{l^3} & \frac{6E_eI_e}{l^2} & 0 & \frac{12E_eI_e}{l^3} & \frac{6E_eI_e}{l^2} \\ 0 & -\frac{6E_eI_e}{l^2} & \frac{2E_eI_e}{l} & 0 & \frac{6E_eI_e}{l^2} & \frac{4E_eI_e}{l} \end{bmatrix} + H_0 \begin{bmatrix} 0 & 0 & 0 & 0 & 0 & 0 \\ 0 & \frac{6}{5l} & -\frac{1}{10} & 0 & -\frac{6}{5l} & -\frac{1}{10} \\ 0 & -\frac{1}{10} & \frac{2l}{15} & 0 & \frac{1}{10} & -\frac{l}{30} \\ 0 & 0 & 0 & 0 & 0 & 0 \\ 0 & -\frac{6}{5l} & \frac{1}{10} & 0 & \frac{6}{5l} & \frac{1}{10} \\ 0 & -\frac{1}{10} & -\frac{l}{30} & 0 & \frac{1}{10} & \frac{2l}{15} \end{bmatrix}. \tag{44}$$

Besides, according to the principle of virtual work, the element stiffness matrix $\mathbf{K}_u$ related to the longitudinal displacement u can be obtained as

$$\mathbf{K}_u = \begin{bmatrix} \frac{EA}{l} & 0 & 0 & -\frac{EA}{l} & 0 & 0 \\ 0 & 0 & 0 & 0 & 0 & 0 \\ 0 & 0 & 0 & 0 & 0 & 0 \\ -\frac{EA}{l} & 0 & 0 & \frac{EA}{l} & 0 & 0 \\ 0 & 0 & 0 & 0 & 0 & 0 \\ 0 & 0 & 0 & 0 & 0 & 0 \end{bmatrix}. \tag{45}$$

The intact element stiffness matrix of a nanowire element thus can be expressed as

$$\mathbf{K}_e = \mathbf{K}_u + \mathbf{K}_w = \begin{bmatrix} \frac{E_eA_e}{l} & 0 & 0 & -\frac{E_eA_e}{l} & 0 & 0 \\ 0 & \frac{12E_eI_e}{l^3} & -\frac{6E_eI_e}{l^2} & 0 & -\frac{12E_eI_e}{l^3} & -\frac{6E_eI_e}{l^2} \\ 0 & -\frac{6E_eI_e}{l^2} & \frac{4E_eI_e}{l} & 0 & \frac{6E_eI_e}{l^2} & \frac{2E_eI_e}{l} \\ -\frac{E_eA_e}{l} & 0 & 0 & \frac{E_eA_e}{l} & 0 & 0 \\ 0 & -\frac{12E_eI_e}{l^3} & \frac{6E_eI_e}{l^2} & 0 & \frac{12E_eI_e}{l^3} & \frac{6E_eI_e}{l^2} \\ 0 & -\frac{6E_eI_e}{l^2} & \frac{2E_eI_e}{l} & 0 & \frac{6E_eI_e}{l^2} & \frac{4E_eI_e}{l} \end{bmatrix} + H_0 \begin{bmatrix} 0 & 0 & 0 & 0 & 0 & 0 \\ 0 & \frac{6}{5l} & -\frac{1}{10} & 0 & -\frac{6}{5l} & -\frac{1}{10} \\ 0 & -\frac{1}{10} & \frac{2l}{15} & 0 & \frac{1}{10} & -\frac{l}{30} \\ 0 & 0 & 0 & 0 & 0 & 0 \\ 0 & -\frac{6}{5l} & \frac{1}{10} & 0 & \frac{6}{5l} & \frac{1}{10} \\ 0 & -\frac{1}{10} & -\frac{l}{30} & 0 & \frac{1}{10} & \frac{2l}{15} \end{bmatrix}. \tag{46}$$

It can be seen from Eq. (46) that the element stiffness matrix has two parts: The first is identical to the classical element stiffness matrix, and the second part is due to the surface residual stress. The stiffness of nanowire is, therefore, increased or decreased depending on the joint action of classic material elasticity and surface effect.

The assembly of element stiffness matrices and nodal force vectors yields the global equilibrium equation as

$$\mathbf{KU} = \mathbf{R}, \tag{47}$$

where **K**, **U**, and **R** denote the global stiffness matrix, global displacement, and global nodal force vector, respectively.

It is worth noting that the obtained element stiffness matrix can only be used to evaluate the mechanical properties of the simply supported beam and fixed–fixed beam. The mechanical property of the cantilever cannot be evaluated by the same finite element method, which is attributed to the existence of the free end on the cantilever. Nonetheless, the proposed finite element model is still innovative and meaningful. Because most struts with specific arrangements in lightweight open-cell nanoscale cellular solids or nanoarchitected metamaterials are simply supported and fixed, while the cantilever is almost nonexistent. Thus, the deflection of the cantilever in Figs. 3 and 4 does not give the corresponding finite element numerical results.

3 Results and discussion

3.1 Effect of surface layer stiffness (SLS)

In this section, the size-dependent effect (ignoring the surface residual stress) is elicited by analyzing the effective Young's modulus of nanowires. We consider a nanowire with a typical circular cross section. Based on Eqs. (3) and (4), effective Young's modulus (E_e) can be simplified as

$$\frac{E_e}{E_b} = \left(1 - \frac{t}{R}\right)^4 + m\left[1 - \left(1 - \frac{t}{R}\right)^4\right], \tag{48}$$

where R and m denote the outer radius of circular cross section and the ratio of surface and bulk Young's modulus (E_s/E_b), respectively. Equation (48) provides a universal relationship for the effective Young's modulus of the nanowire with respect to the relative thickness of the surface layer.

For several representative m (0.2, 0.4, 0.6, 0.8, 1, 1.2, 1.4, 1.6, and 1.8), the theoretical solutions for the effective Young's modulus E_e of nanowires, normalized by the bulk's Young's modulus E_b, are depicted in Fig. 2 as a function of the normalized size R/t. Clearly, effective Young's modulus is controlled by two parameters, i.e., t/R and m. Furthermore, with the decrease in the feature size of the nanowire, normalized size R/t gradually decreases, which leads to the apparent size effect, especially when the normalized size is less than 100. On the contrary, with the increase in the cross-sectional size, normalized size approaches infinite, and the surface effect becomes negligible.

Meanwhile, the increase in parameter m indicates the increase in relative Young's modulus, which leads to the increase in effective Young's modulus. Especially when $m = 1$, the surface Young's modulus is equal to the bulk modulus, which means that surface elasticity does not make an enhanced contribution to effective elasticity. It is worth noting that the normalized Young's modulus sharply increases and decreases with the decrease in the feature size of nanowires for the two different cases of $m > 1$ and $m < 1$, respectively. Also, $m > 1$ stands for a surface layer stiffer than the bulk, $m < 1$ stands for a softer surface, and $m = 1$ indicates that the surface layer has the same Young's modulus as the bulk. This can explain some interesting phenomena from the experiments. For example, with the decrease in the feature size, Young's moduli of Ag, Pb, and ZnO nanowires increase dramatically [60, 87], and those of Cr, CaN, and Si nanowires decrease rapidly [76, 88, 89].

Taking ZnO [60] and GaN [89] as examples, through inverse analysis, the elastic modulus of bulk material, the moduli ratio, and the surface layer thickness of ZnO nanowires are determined as $E_b = 137.1$ GPa, $m = 1.528$, and $t = 4.64$ nm, respectively. Similarly, the material parameters of the GaN nanowires are approximately determined as $E_b = 350$ GPa, $m = 0.208$ and $t = 1.56$ nm, respectively [76]. According to the pattern shown in Fig. 2, as the nanowire size decreases, the size effect of hardening is brought about by m greater than 1 for ZnO nanowires, while the size effect of softening is brought about by m less than 1 for GaN nanowires.

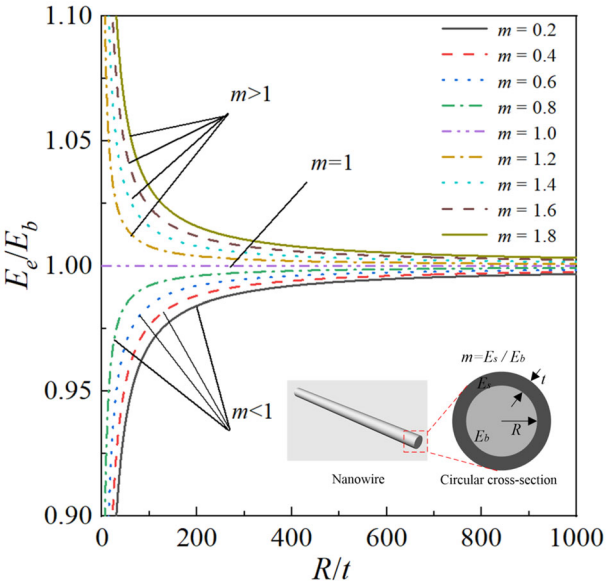

Fig. 2 Normalized Young's moduli E_e/E_b versus normalized size R/t of core–shell nanowires for alternative representative modulus ratios m

3.2 Effect of surface residual stress (SRS)

Based on Gurtin et al.'s theory [54, 55], the bulk component is covered with a thin surface layer, which has a different Young's modulus from bulk value. Predictably, when the thickness of the surface layer approaches zero, the surface effect of nanowires will be dominated by surface residual stress. To study the influence of surface residual stress on the surface effect of nanowires, without the loss of generality, we take the circular cross-sectional silver nanowires as an example. The modeling parameters are $E_s = 0$, $E_b = 76$ GPa, $L = 1$ μm, and $D = 50$ nm, respectively [61]. To eliminate the influence of other factors, as an example, the transverse deflection of the nanowire is directly affected by the external load F, we use the normalized deflection and normalized length to evaluate the mechanical property of the nanowire. Besides, according to the results of Sect. 2.3, a new FEM program based on MATLAB has been employed to compare with the theoretical solution. In the employed FEM program, nanowire was divided into ten elements. To facilitate the collection of data, the transverse deflections of elemental nodes considering the surface effect are automatically calculated by MATLAB and generated into the EXCEL file.

Figure 3a-c shows the theoretical solution and FEM solution of transverse deflection along the longitudinal direction of nanowires with different boundary conditions. In all cases, the deflection direction is consistent with the load direction. As shown in Fig. 3a, the transverse deflection of the cantilever gradually increases with the increase in surface residual stress from 0 to 2 N/m. Compared with the classical case, cantilever nanowire exhibits a soft behavior under the action of surface residual stress. Interestingly, the opposite phenomenon is found in Fig. 3b, c. Specifically, the deflections of simply supported nanowire and fixed-fixed nanowire decrease with the increase in surface residual stress. This indicates that surface residual stress makes simply supported nanowires and fixed–fixed nanowires stiffer. This result is in full agreement with that shown by He et al. [61] in Fig. 3 and verifies the correctness of the theoretical solution in this paper. Furthermore, the excellent agreement between the theoretical solutions and FEM data points verifies the accuracy of the finite element model.

Based on the Young-Laplace equation, the direction of additional force generated by surface residual stress always points to the center of the curvature circle [84]. Due to downward curvature, as shown in Fig. 3a, the direction of transverse distributed force by Eq. (7) must be the same as the direction of the external load F. Thus, the transverse distributed force plays a promotion in the bending deformation of cantilever beams. This indicates that surface residual stress will lead to a material softer behavior on the cantilever. As shown in Fig. 3b, the upward curvature generates an upward transverse distributed force. Because the direction of this transverse distributed force is opposite to that of external load F, the initially downward deflection caused by F is weakened by transverse distributed force, which leads to a material stiffer behavior on simply supported beam. Especially,

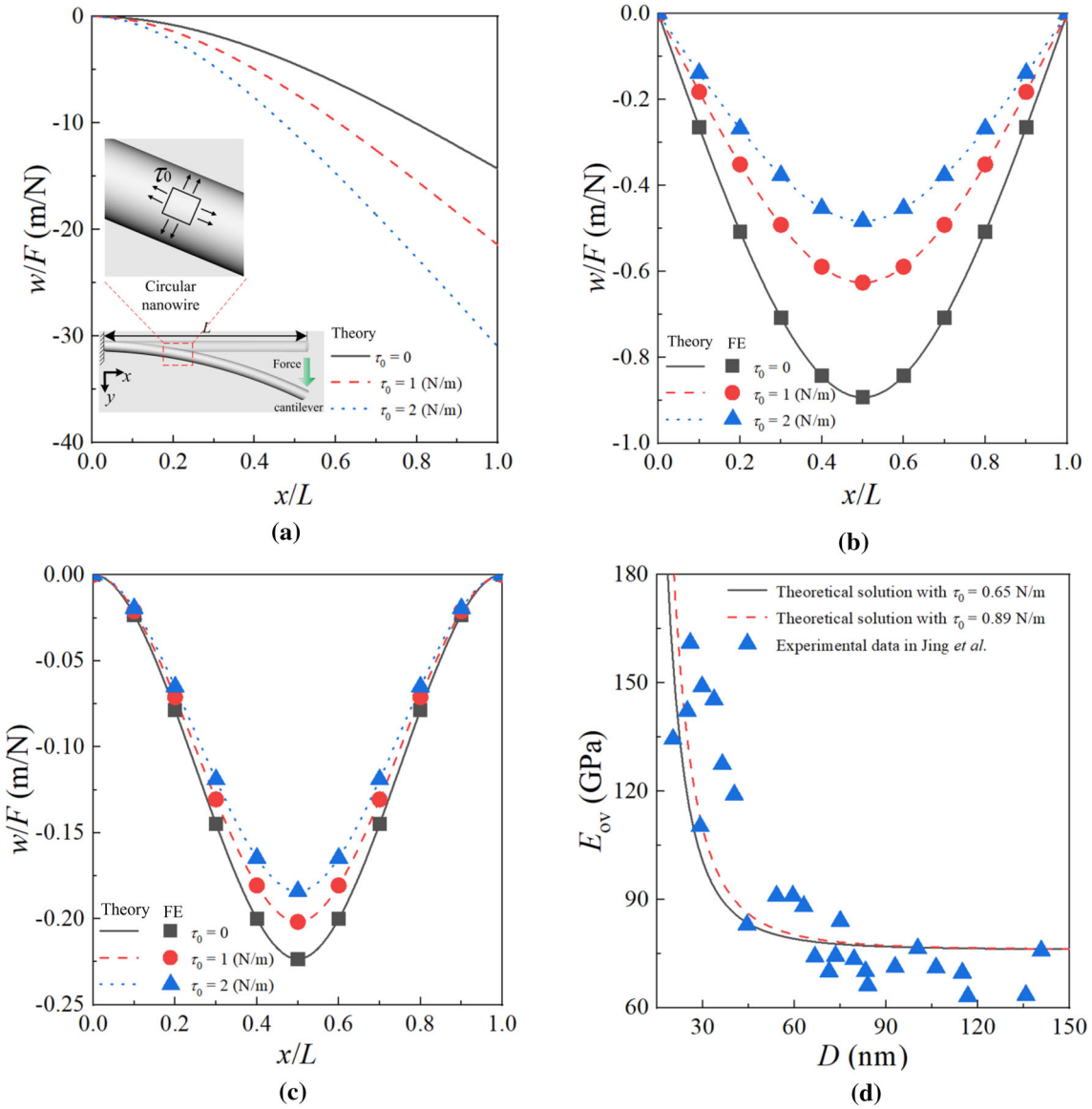

Fig. 3 Theoretical and FEM solution of transverse deflection along the longitudinal direction of nanowires for different boundary conditions: **a** cantilever, **b** simply supported, and **c** fixed–fixed beams, and **d** variation of the overall Young's modulus as a function of the diameters of silver nanowires

the bending curvature shown in Fig. 3c is between Fig. 3a, b. The bending curvature is downward at both ends of the nanowire while upward in the middle of the nanowire. Two symmetrical inflection points must exist between two fixed ends and the middle point of the fixed-fixed beam. Therefore, the transverse distributed force is downward outside of the two inflection points, while it is upward inside the two inflection points. The effect of residual stress on the fixed-fixed nanowire is weaker than simply supported nanowire, which is attributed to the downward transverse distributed force at both fixed boundary offsets a part of deflections. Nevertheless, an apparent stiffer behavior can still be observed near the midpoint of the fixed–fixed nanowire. This shows that the positive influence of surface residual stress on the structural stiffness is dominant compared with the negative influence for the fixed–fixed beam.

To further illustrate the effect of the surface residual stress, the overall Young's modulus has been introduced in this analysis. We assume that a force is applied at the midpoint of the fixed-fixed nanowire (endpoints for cantilever and simply supported boundary conditions) that causes the deflection. Then the force-deflection curves of the nanowire are determined. Following Euler-Bernoulli beam theory, the bending stiffness of the

nanobeam can be inferred from the force and deflection, and subsequently, the overall bending behavior of the nanowire can be obtained. We selected the fixed-fixed nanowire as an example and demonstrated how to obtain the overall Young's modulus. We first gave a force F_e to the fixed-fixed nanobeam at $L/2$ and obtained the deflection w_e at this point by Eq. (18). Next, by bringing F_e and w_e into Eq. (19), we calculated the modulus E_e and defined it as the overall Young's modulus. In this section, the modeling parameters are also set to $E_s = 0$, $E_b = 76$ GPa, $L = 1$ μm. The surface residual stress values of [111] and [001] silver from atomistic calculations of $\tau_0 = 0.65$ N/m or 0.89 N/m were employed, respectively [57]. Besides, the cross section of the silver nanowire is still assumed to be a perfect circle.

Figure 3d shows the overall Young's modulus versus the diameter of silver nanowires. The black straight line and red dash represent the predicted values of overall Young's moduli of silver nanowires by the theoretical method when surface residual stress is set to 0.65 N/m and 0.89 N/m. The blue triangular symbol represents the overall Young's modulus of silver nanowires in Jing et al.'s experiment [90]. As can be seen from Fig. 3d, the trend of E_{ov} versus D is in good agreement with the experimental scatter point from Jing et al.'s experiment, which verifies the accuracy of the employed theoretical model. The general trend of the overall Young's modulus for silver nanowires increases with the decrease in diameter for both the experimental results and the proposed theory. According to the predicted line, when the diameter increases to more than 100 nm, the overall Young's modulus of the silver nanowires tends to a constant of around 76 GPa. This can be utilized to illustrate the size dependence of Young's modulus on microstructure. Although the variable tendency of all curves is similar, the surface residual stress τ_0 plays a vital role regarding the overall Young's modulus E_{ov}. Obviously, increasing the surface residual stress will result in larger values of the overall Young's modulus, which can be explained in Fig. 3c. Because the direction of the main transverse distributed force is opposite to that of external load F near the midpoint, the initially downward deflection caused by F is weakened, which leads to a material stiffer behavior on fixed–fixed silver nanowires. Thus, surface residual stress emerges a positive effect on the overall Young's modulus of the fixed-fixed silver nanowires. Predictably, simply supported nanowire and cantilever nanowire will present the same and opposite trend as a fixed-fixed nanowire.

3.3 The effect of sectional geometry

We plan to give two schemes to study the contribution of cross-sectional geometry on the bending deflection of nanowires. The first configuration is to strictly limit the cross section of the nanowire to a circumscribed circle of a specific size. We utilize this configuration to evaluate the overall influence of the cross-sectional geometry on the bending deflection of the nanowires even though the increase or decrease in deflection cannot reflect the enhancement or weakening of surface effect due to the change of the cross section shape of nanowires. For example, when the cross-sectional shape of nanowire changes concerning the same circumscribed circle, it does not only affect the surface effect but also affect the cross-sectional area of nanowires. Thus, the second configuration is to keep the cross-sectional area of the nanowire constant, so that the size of the circumscribed circle corresponding to different cross-sectional geometry will be different. The purpose of this deployment is to better evaluate the influence of surface effects caused by the cross-sectional geometry on the bending deflection of nanowires by eliminating the cross-sectional area factor.

The theoretical solution and FEM solution of transverse deflection along the longitudinal direction of nanowires for several representative cross sections ($n = 4$, 6, 8, 10, 12, 14, 16, and 18) are plotted in Fig. 4, where two top figures, two middle figures, and two below figures represent cantilever, simply supported beam and fixed-fixed beam, respectively. In addition, the three figures on the left in Fig. 4 represent the first configuration, while the three figures on the right represent the second configuration (the subfigures are partial enlargement of the dashed box). Differing from Sects. 3.1 and 3.2, both the surface residual stress and surface layer stiffness are considered in this section. We take the following representative material parameters: $L = 1$ μm, $\tau_0 = 1$ N/m, $E_b = 76$ GPa, and $m = E_s/E_b = 1.5$. The diameter D of the circumscribed circle in the first configuration is given as a constant of 50 nm, while D in the second configuration is completely in accordance with the data in Table 1. To facilitate the comparison with the first configuration, all the cross sections in Table 1 maintain the same area, which is equal to the area of a circle with a diameter of 50 nm. The tendencies of transverse deflection along the longitudinal direction of nanowires with different boundary conditions in Fig. 4 are similar to the ones shown in Fig. 3a–c. In addition, the finite element solution is in good agreement with the theoretical solution in Fig. 4c–f, which further verifies the accuracy of the finite element program developed in this paper. Comparing the left and right images in Fig. 4, we find that all the curves in the left images are more divergent, while all the curves in the right images are more concentrated. This shows that the cross-sectional

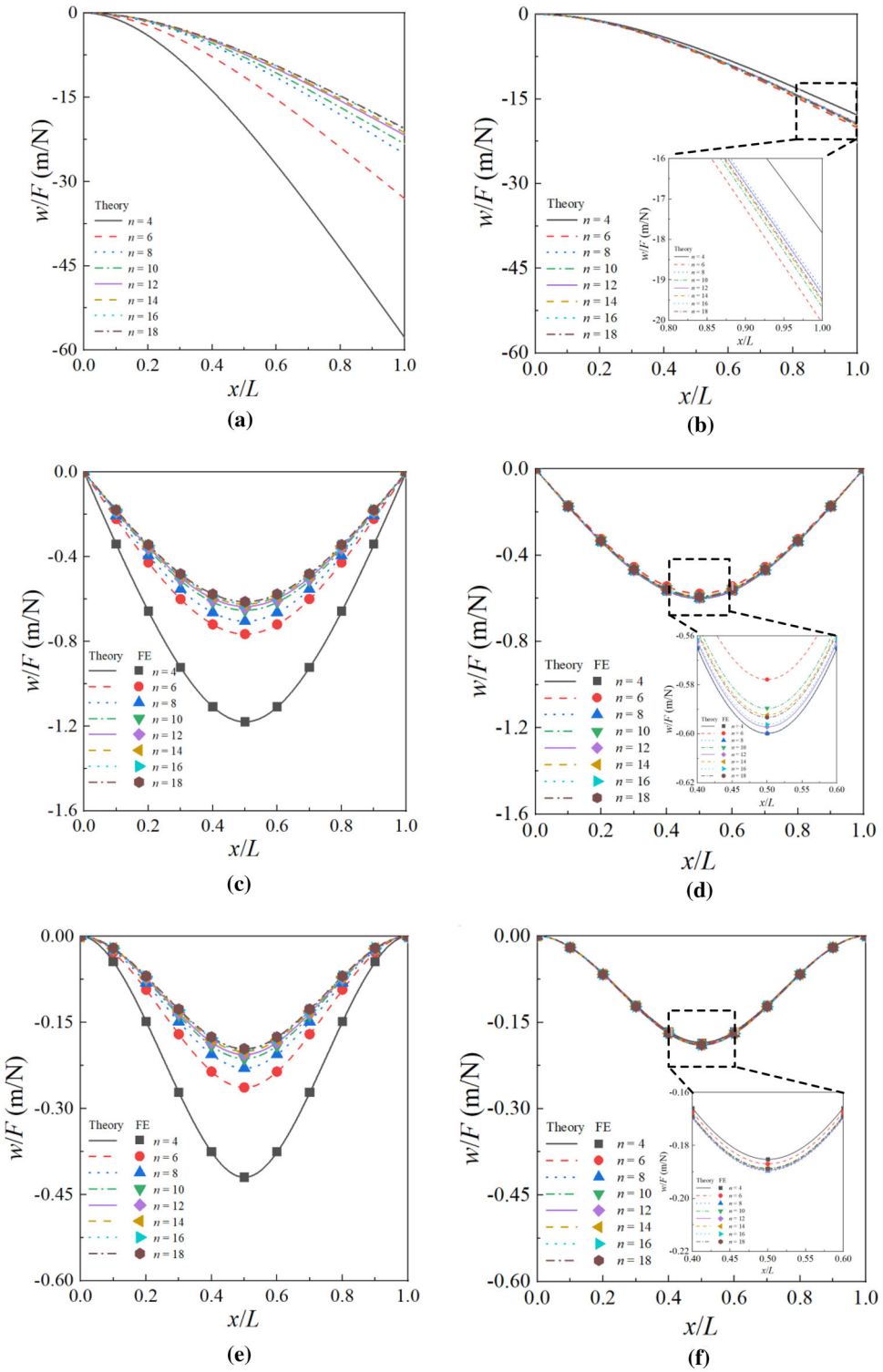

Fig. 4 Theoretical and FEM solutions of normalized transverse deflection along the longitudinal direction of nanowires with the first configuration (left figures) and second configuration (right figures) for several representative cross sections ($n = 4$, 6, 8, 10, 12, 14, 16, and 18) with different boundary conditions: **a**, **b** cantilever; **c**, **d** simply supported, and **e**, **f** fixed–fixed beams

Table 1 Circumscribed circle diameter of different regular polygons in the second configuration

n	4	6	8	10	12	14	16	18
D (nm)	62.6657	54.9818	52.6954	51.6952	51.1663	50.8521	50.6501	50.5124

area has a more significant influence on the deflection of the nanowire than the cross-sectional geometry. In addition, we have confined the cross section of the nanowire strictly to the same outer circle in Fig. 4a, c, e, which results in a transverse deflection that is strongly influenced by the area. Thus, the transverse deflection exhibits a monotonic variation with n. Nevertheless, in Fig. 4b, d, f, to eliminate the effect of cross-sectional area, we set the nanowire cross-sectional area to a constant value in all cases. From Eq. (9) in the manuscript, it is clear that intermediate parameter H is a segmented function with respect to n, which causes the transverse deflection of the nanowire not to exhibit apparent monotonicity with n. Despite all this, as n increases, the transverse deflection of the nanowires still shows a convergence trend, which is verified in Fig. 5.

To more clearly describe the influence of the cross-sectional shape on the transverse deflection of the nanowire, scatter plots with the representative cross sections ($n = 4, 6, 8, 10, 12, 14, 16$, and 18) as the abscissa and the absolute value of theoretical maximum normalized transverse deflection in Fig. 4 as the coordinates are shown in Fig. 5. Here again, in order to eliminate the effect of the cross-sectional area, in addition to the transverse deflection divided by the loading force (Fig. 5a–c), the transverse deflection divided by the cross-sectional area of the nanowires (Fig. 5d–f) is also used as a normalized transverse deflection. The red square scatter points represent the first configuration, while the blue circle scatter points represent the second configuration. It is found in Fig. 5 that the cross-sectional geometry influences the transverse deflection of nanowires. Specifically, for the first configuration, with the increased side number n, all the maximum transverse deflection in all three boundary conditions decreases gradually. For the same circumscribed circle, therefore, the maximum transverse deflection of the nanowire with a square cross section is most significant, and it is minimal for $n = 18$. Nevertheless, it is impossible that the maximum deflection of the nanowires decreases infinitely with the increased side number n. For example, the ultimate normalized deflection of nanowires tends to 19.411 for cantilever. This is because the cross-sectional shape of the nanowire becomes a circle when n tends to infinity. Once the shape of the nanowire cross section is determined, its transverse deflection is also determined. Interestingly, the absolute value of theoretical maximum normalized transverse deflection in the second configuration does not show decreases monotonically with the increase in the edge number of the regular polygon as in the first configuration. Although the blue circle scatter points in Fig. 5 show upward and downward fluctuations, we can still find some regularity by observing the deflection with the number of sides $4a$ and $4a + 2$ separately. Specifically, with the increase in a, the deflection with the number of sides $4a$ shows a monotonic increase, while the deflection with the number of sides $4a + 2$ shows a monotonic decreasing trend, in Fig. 5a, d. Even though the blue scatter points eventually stabilize to a constant deflection, which depends on the circular section of the same cross-sectional area. The fluctuation law of the blue scattered points in Fig. 5b, e is just the opposite of that in Fig. 5a, d. This is because the residual stress makes the hardness of the cantilever and the simply supported beam show the opposite trend. Separately observing the red and blue scatter points in Fig. 5c, f, we can find the trend with the fixed–fixed boundary conditions can be regarded as a superposition of a cantilever beam and a simply supported beam. This corresponds again to the conclusion obtained in Sect. 3.2.

3.4 The competitive mechanism of SLS and SRS

To avoid confusion, let us review the definitions related to Young's modulus before starting this section. E_b and E_s are defined as the Young's modulus of the bulk material and the surface layer, which is the basis of the other moduli. E_0 and E_e are defined as effective surface Young's modulus and effective Young's modulus. Specifically, effective surface Young's modulus E_0 is equal to $E_s t$ and the unit is N/m, which is different from Young's modulus in the general sense. Effective Young's modulus E_e is equal to $(E_b I_b + E_s I_s)/I_e$, which is a variable related to the Young's modulus of the sub-material and the cross-sectional geometry of the nanowire, but not related to the surface residual stress and boundary conditions. E_{ov} is defined as overall Young's modulus and same as the meaning we gave before. Actually, the overall Young's modulus is a physical quantity obtained from experiments: first load the nanowire to make it bend and deform, then measure the maximum deflection (the rightmost end of the cantilever beam, the middle position of the simply supported beam and the fixed-fixed

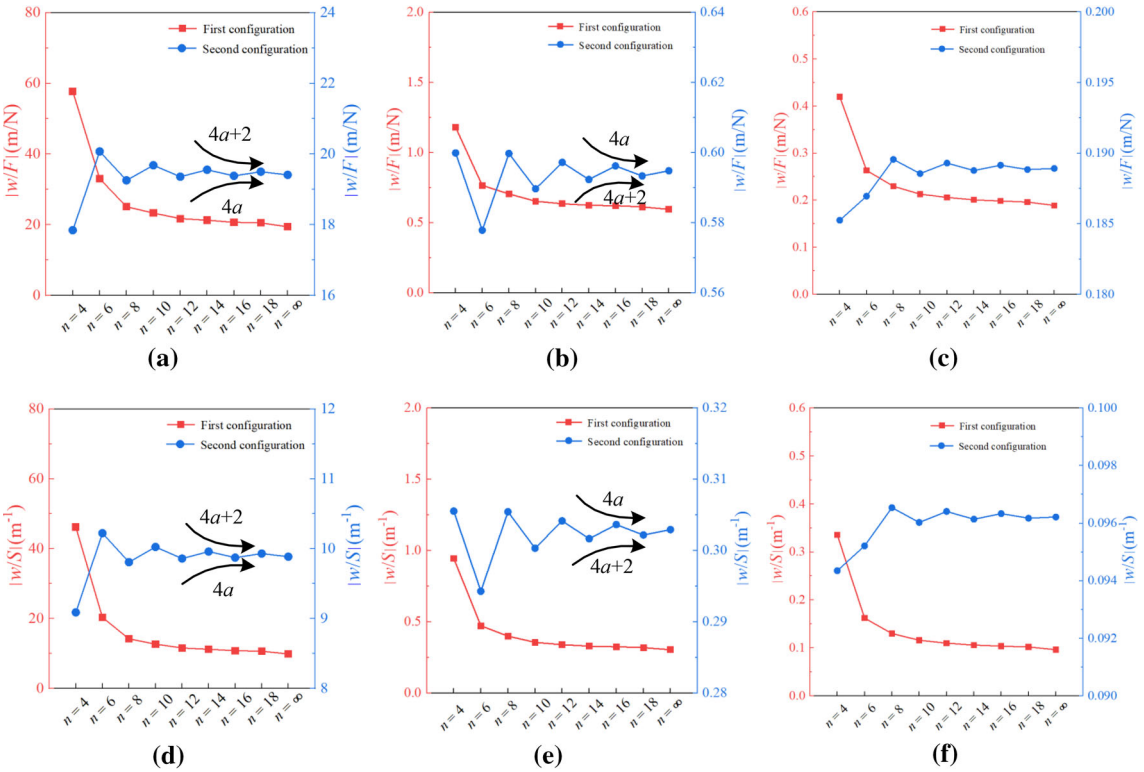

Fig. 5 Absolute value of theoretical maximum normalized transverse deflection versus several representative cross sections ($n =$ 4, 6, 8, 10, 12, 14, 16, and 18) with two configurations for different boundary conditions: **a**, **d** cantilever, **b**, **e** simply supported beam, and **c**, **f** fixed–fixed beams

beam), and finally assume a nanowire with the same maximum deflection without considering the surface effect, use the classic elastic bending theory to deduce the overall Young's modulus. Without ignoring the thickness of the surface layer, the overall Young's modulus is a physical quantity that comprehensively considers the surface residual stress and surface layer stiffness of the nanowires.

The normalized Young's moduli E_{ov}/E_b and E_{ov}/E_e are employed here to evaluate the competitive mechanism of SLS and SRS. Figure 6 shows the normalized Young's moduli E_{ov}/E_b (a, b, and c) and E_{ov}/E_e (d, e and f) versus the normalized sizes R/t of nanowires for several represent cross sections ($n = 4$, 6, 8, 10, 12, 14, 16, and 18) with different boundary conditions. The same material parameters as above are set here. It is worth noting that two different normalized Young's moduli must be distinguished, which is attributed to the purpose of evaluating the competitive mechanism of SLS and SRS. Specifically, normalized Young's moduli E_{ov}/E_b includes the joint influence of surface layer stiffness and surface residual stress, while normalized Young's moduli E_{ov}/E_e only includes the influence of surface residual stress. It is necessary to point out that according to the calculation rule of E_{ov} proposed in Sect. 3.2, the influence of the cross-sectional area on the deformation of nanowires has been eliminated for either normalized Young's modulus (E_{ov}/E_b or E_{ov}/E_e).

To get a good view of the effect of the number of nanowire cross-sectional edges n on the normalized Young's moduli, we therefore restrict the values of the vertical coordinates in Fig. 6 to a pretty range, e.g., $1 < E_{ov}/E_b < 1.02$. Such a setup results in a size effect of the nanostructure that is not very significant. Therefore, Table 2 adds to quantify the contribution of size effects to the normalized Young's moduli. It is seen that in Table 2, the Young's moduli of the nanowires show a distinct size effect when their feature size reduces to nanometers, especially at R/t less than 100. Specifically, both normalized Young's moduli E_{ov}/E_b and E_{ov}/E_e of cantilever gradually decrease with the decrease in the feature size, while the opposite trend is for simply supported beam and fixed–fixed beam. Meanwhile, with the increase in the feature size, both normalized Young's moduli E_{ov}/E_b and E_{ov}/E_e of cantilever gradually approach 1 for nanowires with any boundary conditions. This phenomenon confirms the above conclusion once again that the surface effect reduces the stiffness of the cantilever beam and increases the stiffness of the simply supported beam and fixed–fixed beam. Comparing Fig. 6a, d, the results show the curve in Fig. 6a has an inverted "V"-type trend of firstly increasing and then decreasing. In

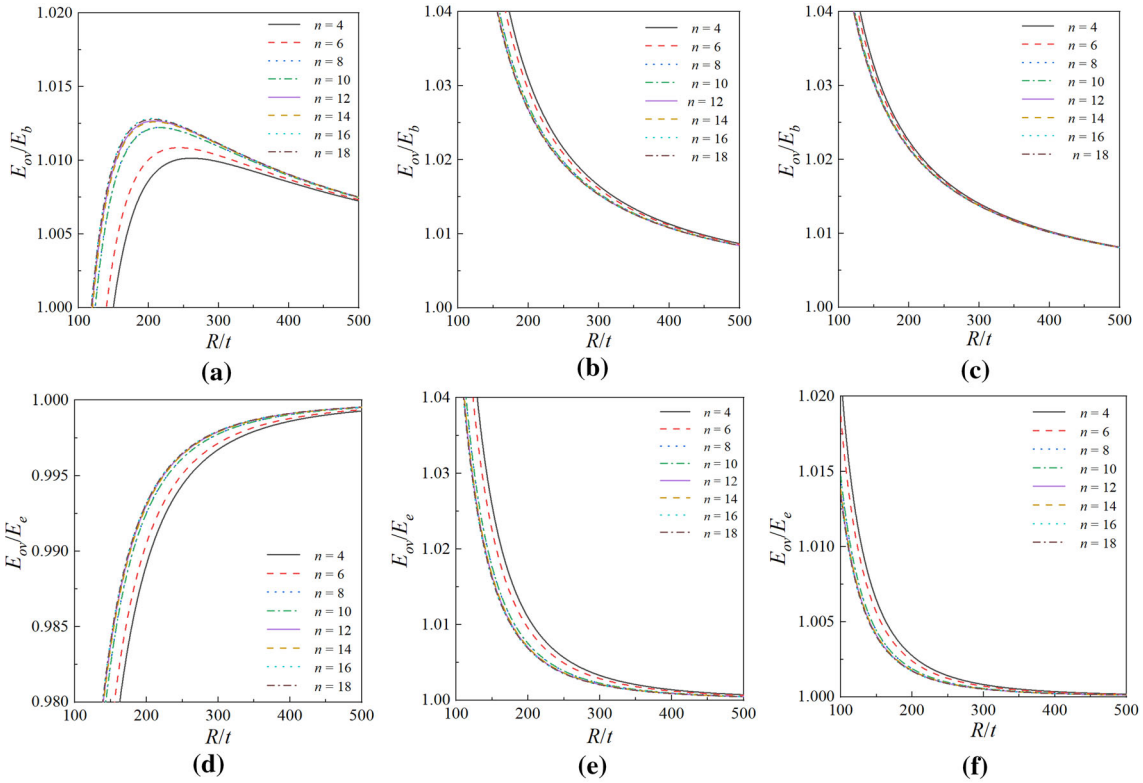

Fig. 6 Normalized Young's moduli E_e/E_b (**a**, **b**, and **c**) and E_{ov}/E_e (**d**, **e**, and **f**) versus the normalized sizes R/t of nanowires for several represent cross sections ($n = 4$, 6, 8, 10, 12, 14, 16, and 18) with different boundary conditions: **a**, **d** cantilever, **b**, **e** simply supported beam, and **c**, **f** fixed–fixed beam

the meantime, the contour typically rises monotonically in Fig. 6d. This implies a competitive mechanism in the process of the surface residual stress and surface layer stiffness affecting the deformation of nanowires. To further illustrate the problem, an intermediate parameter Δ is introduced according to the following formula, to represent the contribution of the surface residual stress and surface layer stiffness on the overall Young's modulus of nanowires:

$$\Delta = \begin{cases} \frac{E_{ov}}{E_e} - 1 & \text{(Surface residual stress)}, \\ \frac{E_{ov}}{E_b} - \frac{E_{ov}}{E_e} & \text{(Surface layer stiffness)}. \end{cases} \tag{49}$$

In Eq. (49), the first formula only denotes the contribution of the surface residual stress on the overall Young's modulus of nanowires, while the second formula only denotes the contribution of the surface layer stiffness on the overall Young's modulus of nanowires. Moreover, a positive Δ indicates a stiffer effect on the nanowire, while a negative Δ indicates a softer effect, and the greater the absolute value of Δ represents the greater the influence on material stiffness. Take a square cross-sectional cantilever as an example; intermediate parameter Δ concerning the surface residual stress, surface layer stiffness, and their difference are shown in Fig. 7a. As can be seen in Fig. 7a, under the selected material parameters ($\tau_0 = 1$ N/m and $m = 1.5$), the surface residual stress reduces the overall Young's modulus of the nanowire, and the Δ of the surface residual stress increases with the feature size. This indicates a reduction in the influence of surface residual stress was observed with the increase in feature size. On the other hand, the surface layer stiffness lifts the overall Young's modulus of the nanowire. The Δ of the surface residual stress decreases with the increase in feature size. This also donates an attenuated effect of surface layer stiffness with increasing feature size.

The difference between the surface residual stress and surface layer stiffness can clearly inflect their competitive relationship. As shown in the right coordinate of Fig. 7a, two characteristic points divide the solid red line into three stages. In the first stage, a negative difference indicates the softer effect of surface residual stress is greater than the stiffer effect of surface layer stiffness on overall Young's modulus. When the feature

Table 2 The normalized Young's moduli E_{ov}/E_b and E_{ov}/E_e of cantilever, simply supported beam, and fixed–fixed beam

E_{ov}/E_b of cantilever								
R/t	n							
	4	6	8	10	12	14	16	18
20	0.00478	0.00806	0.01825	0.01803	0.02267	0.02199	0.02440	0.02379
70	0.83071	0.85597	0.89462	0.89406	0.90462	0.90322	0.90798	0.90684
120	0.98244	0.98872	0.99799	0.99786	1.00032	1.00000	1.00110	1.00084
E_{ov}/E_e of cantilever								
R/t	n							
	4	6	8	10	12	14	16	18
20	0.00408	0.00688	0.01557	0.01539	0.01934	0.01876	0.02082	0.02030
70	0.78760	0.81155	0.84819	0.84766	0.85767	0.85634	0.86086	0.85977
120	0.95151	0.95759	0.96657	0.96644	0.96883	0.96851	0.96958	0.96932
E_{ov}/E_b of simply supported beam								
R/t	n							
	4	6	8	10	12	14	16	18
20	11.70148	10.38226	8.44336	8.47092	7.95605	8.02381	7.79326	7.84858
70	1.31440	1.28097	1.23213	1.23282	1.21992	1.22162	1.21585	1.21724
120	1.08417	1.07750	1.06778	1.06791	1.06535	1.06568	1.06453	1.06481
E_{ov}/E_e of simply supported beam								
R/t	n							
	4	6	8	10	12	14	16	18
20	9.98463	8.85896	7.20454	7.22805	6.78873	6.84654	6.64982	6.69702
70	1.24618	1.21449	1.16818	1.16884	1.15661	1.15822	1.15275	1.15406
120	1.05003	1.04358	1.03416	1.03429	1.03180	1.03213	1.03102	1.03128
E_{ov}/E_b of fixed–fixed beam								
R/t	n							
	4	6	8	10	12	14	16	18
20	3.90032	3.55396	3.04582	3.05303	2.91836	2.93608	2.87581	2.89027
70	1.11979	1.11140	1.09915	1.09933	1.09609	1.09652	1.09507	1.09542
120	1.04543	1.04376	1.04133	1.04136	1.04072	1.04081	1.04052	1.04059
E_{ov}/E_e of fixed–fixed beam								
R/t	n							
	4	6	8	10	12	14	16	18
20	3.32806	3.03251	2.59893	2.60509	2.49018	2.50529	2.45387	2.46620
70	1.06168	1.05372	1.04211	1.04227	1.03921	1.03961	1.03824	1.03857
120	1.01251	1.01090	1.00854	1.00857	1.00795	1.00803	1.00776	1.00782

size is greater than 150, the curve goes into the second stage. At this time, surface layer stiffness beats surface residual stress and occupies the dominant position. When the feature size is around 260, the difference gets the maximum. The point (260, 0.014) corresponds to the vertex of the black "V"-typical curve in Fig. 6a. With the further increase in feature size, the effect of surface residual stress and surface layer stiffness becomes less and less significant, and therefore, both the normalized modulus E_{ov}/E_b and E_{ov}/E_e tend to 1. A similar mechanism can be utilized to explain the cases of simply supported beam and fixed-fixed beam. Differing from the cantilever, both the surface residual stress and surface layer stiffness improve the overall Young's modulus of the nanowires for simply supported beam and fixed–fixed beam. Thus, the normalized modulus

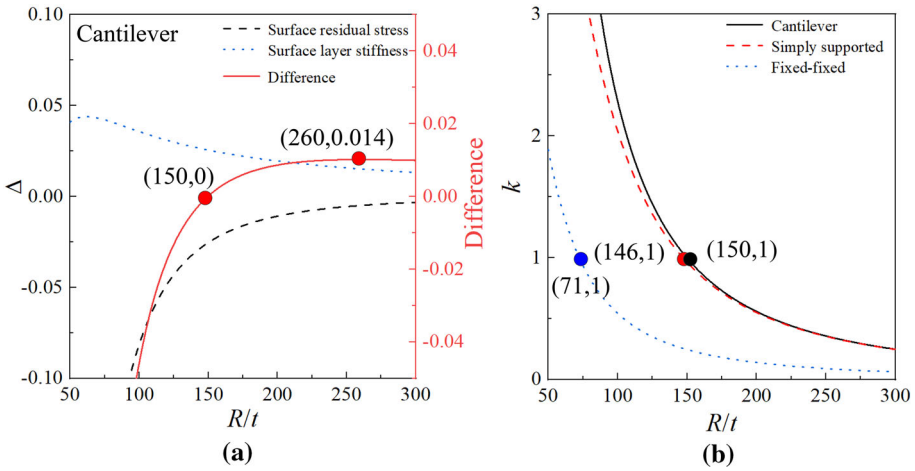

Fig. 7 Relationships of: **a** intermediate parameter Δ and **b** coefficient k with normalized size R/t

E_{ov}/E_b is always greater than the normalized modulus E_{ov}/E_e corresponding to the same feature size for simply supported beam in Fig. 6b, e and fixed-fixed beam in Fig. 6d, f.

To compare the influence of different boundary conditions on this competitive mechanism, another coefficient k is introduced according to the following formula:

$$k = \left| \frac{\frac{E_{ov}}{E_e} - 1}{\frac{E_{ov}}{E_b} - \frac{E_{ov}}{E_e}} \right|. \tag{50}$$

According to the relationship in Eq. (50), if the coefficient k is greater than 1, the influence of the surface residual stress on Young's modulus is greater than surface layer stiffness. Figure 7b shows the relationships of coefficient k with normalized size R/t for different boundary conditions. Similar feature points can be found in the simply supported beam and fixed-fixed beam simultaneously. With the strengthening of boundary constraints, the critical normalized size (the horizontal coordinates corresponding to the solid circle points in Fig. 7b) gradually decreases. The feature size corresponding to the critical nominalized size is the critical feature size. It also means for nanowires of the same feature size, the stronger the boundary constraint, the more obvious the effect of surface layer stiffness on overall Young's modulus. This discovery may bring inspiration to the research of the nanoelectromechanical system.

Figure 8 shows the variation of the normalized Young's moduli E_{ov}/E_b and E_{ov}/E_e of nanowires with several representative cross sections when the normalized size is 50. As can be seen from Fig. 8, the cross-sectional geometry of a nanowire influences the size effect of its overall elastic property. With the increase in the side number n, both normalized Young's moduli E_{ov}/E_b and E_{ov}/E_e do not show a monotonic trend reported by Zheng [76]. For example, the order of normalized modulus E_e/E_b from small to large in Fig. 8a is as follows: $n = 4$, 6, 10, 8, 14, 12, 18, and 16. This is because only the surface layer stiffness was considered while the surface residual stress was ignored in Zheng's [76] study about the cross-sectional shape of nanowires. From Eqs. (18) and (19), the conjoint contributions of both surface residual stress and surface layer stiffness affect overall Young's modulus. Nevertheless, a general growth and reduction trend of normalized moduli with the increased side number n can still be captured in cantilever and simply supported beam (or fixed–fixed beam), respectively. For a specified normalized size, therefore, the effect for the nanowire with square cross section is the most significant and it is minimal for circular nanowire.

In this paper, we have focused on the surface effect associated with surface elasticity. The contributions of surface residual stress and surface layer stiffness to the size effect of the nanowire have been discussed in details. Remarkably, reported findings in the literature about the effect of these contributions have been contradictory. For example, Zheng et al. [76], and Fen [63] implied that the surface layer stiffness is the most important factor for the size effect relative to the surface residual stress. However, the opposite views were proposed by Goudarzi et al. [77], Moshtaghin et al. [78], and Liu et al. [47]. It is found in this paper that the size effect of the nanowire is affected by both the surface residual stress and the surface layer stiffness. The dominant mechanism depends on the feature size of nanowires. It is important to mention that several other

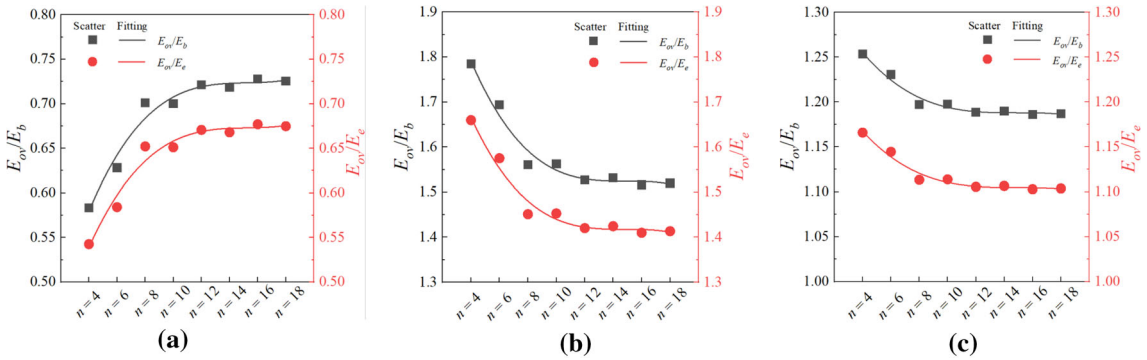

Fig. 8 Normalized Young's moduli E_{ov}/E_b and E_{ov}/E_e versus several representative cross sections ($n = 4$, 6, 8, 10, 12, 14, 16, and 18) with different boundary conditions: **a** cantilever, **b** simply supported, and **c** fixed–fixed beam

factors may also influence the size effect of nanowire deformation, e.g., anisotropy [84], surface roughness, and crystalline defects.

4 Concluding remarks

In summary, we introduce a theoretical method based on the Young-Laplace equation and Euler–Bernoulli beam theory to study the surface effects of nanowire structures. Subsequently, a new finite element model based on Galerkin's weighted residual method is developed to verify the accuracy of the theoretical solution. This paper conducts a systematic study to explore the potentiation mechanism of the surface residual stress and surface layer stiffness on the mechanical properties of nanowires. The research leads to the following principal findings:

(1) When the surface residual stress is neglected, the surface effect of nanowires is found to be closely related to the ratio m of the surface Young's modulus and bulk Young's modulus. Specifically, the effective Young's modulus increases with m and shows a significant size dependence. When m is greater than 1, the effective Young's modulus increases as the normalized size decreases. The opposite trend is observed when m is less than 1. The size dependence becomes very obvious when the normalized size is less than 100 and has no obvious relationship with the boundary conditions.

(2) When the nanowires are regarded as the simplified models that ignore the surface skin, both the transverse deflection and overall Young's modulus are found to be significantly affected by the surface residual stress and boundary conditions. Specifically, the surface residual stress leads the simply supported beam and fixed-fixed beam stiffer, however makes the cantilever softer. The calculation result of the finite element program verifies the correctness of the theoretical solution very well. In addition, the silver nanowires are used as an example to predict the relationship between the overall Young's modulus and the sectional diameter through the theoretical method, and the predicted results correspond well to the experimental values.

(3) The sectional geometry of the nanowires also has a noticeable impact on their transverse deflection. If the circumscribed circle of the cross section remains constant, the nanowires become harder and harder as the numbers of sectional sides increase under specific feature size and boundary conditions. If the cross-sectional area keeps constant, the deflection of the nanowires fluctuates as the number of cross-sectional sides increase. However, it will finally stabilize at a value equivalent to the deflection of the circular cross-sectional nanowire.

(4) When considering the surface residual stress and surface layer stiffness at the same time, we are surprised to find that the overall Young's modulus of nanowires is closely related to the feature size. When the cross-sectional feature size is below the critical feature size, the surface residual stress dominates the bending behavior of the nanowire. As the sectional feature size increases to be larger than the critical feature size, the dominant factor also gradually transforms from the surface residual stress to surface layer stiffness. This critical feature size is closely related to the boundary condition of nanowires. The critical normalized size of the fixed–fixed silver beam is about 71, while it is 146 and 150 for the cantilevered silver beam and simply supported silver beam, respectively.

Acknowledgements We acknowledge the support from the National Natural Science Foundation of China (Grant Numbers 11872149 and 12072072) and China Scholarship Council. A.H. Akbarzadeh acknowledges the financial support by Natural Sciences and Engineering Research Council of Canada through NSERC Discovery Grant (RGPIN-2016-0471) and Canada Research Chairs program in Multifunctional Metamaterials.

Funding This study was funded by the National natural science foundation of China, 11872149, Changwen Mi, 12072072, Changwen Mi, China scholarship council, 202006090226, Yongchao Zhang, natural sciences and engineering research council of Canada, RGPIN-2016-0471, Abdolhamid Akbarzadeh, Canada research chairs, Multifunctional Metamaterials, Abdolhamid Akbarzadeh.

References

1. Maskery, I., Aboulkhair, N.T., Aremu, A.O., Tuck, C.J., Ashcroft, I.A.: Compressive failure modes and energy absorption in additively manufactured double gyroid lattices. Add. Manuf. **16**, 24–29 (2017)
2. Mueller, J., Raney, J.R., Shea, K., Lewis, J.A.: Architected lattices with high stiffness and toughness via multicore-shell 3D printing. Adv. Mater. **30**, e1705001 (2018)
3. Chen, Y., Li, T., Jia, Z., Scarpa, F., Yao, C.-W., Wang, L.: 3D printed hierarchical honeycombs with shape integrity under large compressive deformations. Mater. Des. **137**, 226–234 (2018)
4. Kruk, S., Kivshar, Y.: Functional meta-optics and nanophotonics governed by mie resonances. ACS Photon. **4**, 2638–2649 (2017)
5. Brunet, T., Leng, J., Mondain-Monval, O.: Materials science. Soft acoustic metamaterials. Science **342**, 323–324 (2013)
6. Wang, Q., Jackson, J.A., Ge, Q., Hopkins, J.B., Spadaccini, C.M., Fang, N.X.: Lightweight mechanical metamaterials with tunable negative thermal expansion. Phys. Rev. Lett. **117**, 175901 (2016)
7. Akselrod, G.M., Argyropoulos, C., Hoang, T.B., Ciracì, C., Fang, C., Huang, J., et al.: Probing the mechanisms of large Purcell enhancement in plasmonic nanoantennas. Nat. Photon. **8**, 835–840 (2014)
8. Babaee, S., Shim, J., Weaver, J.C., Chen, E.R., Patel, N., Bertoldi, K.: 3D soft metamaterials with negative Poisson's ratio. Adv. Mater. **25**, 5044–5049 (2013)
9. Shi, J., Mofatteh, H., Mirabolghasemi, A., Desharnais, G., Akbarzadeh, A.: Programmable multistable perforated shellular. Adv. Mater. **33**, e2102423 (2021)
10. Yuan, S., Chua, C.K., Zhou, K.: 3D-printed mechanical metamaterials with high energy absorption. Adv. Mater. Technol. **4**, 1800419 (2019)
11. Shi, J., Akbarzadeh, A.H.: Hierarchical cellular ferroelectric metamaterials: A design motif to enhance multifunctional figures of merit. Comp. Struct. **250**, 112395 (2020)
12. Cui, Y., Zhong, Z.H., Wang, D.L., Wang, W.U., Lieber, C.M.: High performance silicon nanowire field effect transistors. Nano Lett. **3**, 149–152 (2003)
13. He, Z., Yang, Y., Liang, H.W., Liu, J.W., Yu, S.H.: Nanowire genome: a magic toolbox for 1D nanostructures. Adv. Mater. **31**, 51 (2019)
14. Chen, W.S., Jiang, J.Y., Zhang, W.L., Wang, T., Zhou, J.F., Huang, C.H., et al.: Silver nanowire-modified filter with controllable silver ion release for point-of-use disinfection. Environ. Sci. Technol. **53**, 7504–7512 (2019)
15. Meille, S., Lombardi, M., Chevalier, J., Montanaro, L.: Mechanical properties of porous ceramics in compression: on the transition between elastic, brittle, and cellular behavior. J. Eur. Ceram. Soc. **32**, 3959–3967 (2012)
16. Fiedler, T., Ochsner, A., Gracio, J., Kuhn, G.: Structural modeling of the mechanical behavior of periodic cellular solids: open-cell structures. Mech. Compos. Mater. **41**, 277–290 (2005)
17. Liu, L., Chen, Y.J., Liu, H.Z., Rehman, H.U., Chen, C., Kang, H.M., et al.: A graphene oxide and functionalized carbon nanotube based semi-open cellular network for sound absorption. Soft Matter **15**, 2269–2276 (2019)
18. Zhang, C.Y., Akbarzadeh, A., Kang, W., Wang, J.X., Mirabolghasemi, A.: Nano-architected metamaterials: carbon nanotube-based nanotrusses. Carbon **131**, 38–46 (2018)
19. Zhang, X., Vyatskikh, A., Gao, H.J., Greer, J.R., Li, X.Y.: Lightweight, flaw-tolerant, and ultrastrong nanoarchitected carbon. Proc. Natl. Acad. Sci. USA **116**, 6665–6672 (2019)
20. Meza, L.R., Zelhofer, A.J., Clarke, N., Mateos, A.J., Kochmann, D.M., Greer, J.R.: Resilient 3D hierarchical architected metamaterials. Proc. Natl. Acad. Sci. USA **112**, 11502–11507 (2015)
21. Kadic, M., Milton, G.W., van Hecke, M., Wegener, M.: 3D metamaterials. Nat. Rev. Phys. **1**, 198–210 (2019)
22. Milton, G.W.: Complete characterization of the macroscopic deformations of periodic unimode metamaterials of rigid bars and pivots. J. Mech. Phys. Solids **61**, 1543–1560 (2013)
23. Bauer, J., Meza, L.R., Schaedler, T.A., Schwaiger, R., Zheng, X.Y., Valdevit, L.: Nanolattices: an emerging class of mechanical metamaterials. Adv. Mater. **29**, 40 (2017)
24. Bertoldi, K., Vitelli, V., Christensen, J., van Hecke, M.: Flexible mechanical metamaterials. Nat. Rev. Mater. **2**, 17066 (2017)
25. Schaedler, T.A., Jacobsen, A.J., Torrents, A., Sorensen, A.E., Lian, J., Greer, J.R., et al.: Ultralight metallic microlattices. Science **334**, 962–965 (2011)
26. Zheng, X.Y., Lee, H., Weisgraber, T.H., Shusteff, M., DeOtte, J., Duoss, E.B., et al.: Ultralight, ultrastiff mechanical metamaterials. Science **344**, 1373–1377 (2014)
27. Bauer, J., Hengsbach, S., Tesari, I., Schwaiger, R., Kraft, O.: High-strength cellular ceramic composites with 3D microarchitecture. Proc. Natl. Acad. Sci. USA **111**, 2453–2458 (2014)
28. Sarvestani, H.Y., Akbarzadeh, A.H., Mirbolghasemi, A., Hermenean, K.: 3D printed meta-sandwich structures: failure mechanism, energy absorption and multi-hit capability. Mater. Des. **160**, 179–193 (2018)
29. Baughman, R.H.: Avoiding the shrink. Nature **425**, 667 (2003)

30. Gibson, L.J., Ashby, M.F., Schajer, G.S., Robertson, C.I.: The mechanics of two-dimensional cellular materials. Proc. Roy. Soc. Lond. Mater. **382**, 25–42 (1982)
31. Fang, X.Q., Zhu, C.S., Liu, J.X., Liu, X.L.: Surface energy effect on free vibration of nano-sized piezoelectric double-shell structures. Phys. B **529**, 41–56 (2018)
32. Fan, T.: Nano porous piezoelectric energy harvester by surface effect model. Mech. Adv. Mater. Struct. **27**, 754–760 (2020)
33. Xu, F.F., Fang, F.Z., Zhu, Y.Q., Zhang, X.D.: Study on crystallographic orientation effect on surface generation of aluminum in nano-cutting. Nanoscale Res. Lett. **12**, 289 (2017)
34. Xia, W., Mahmood, A., Zou, R.Q., Xu, Q.: Metal-organic frameworks and their derived nanostructures for electrochemical energy storage and conversion. Energy Environ. Sci. **8**, 1837–1866 (2015)
35. Kaneti, Y.V., Tang, J., Salunkhe, R.R., Jiang, X.C., Yu, A.B., Wu, K.C.W., et al.: Nanoarchitectured design of porous materials and nanocomposites from metal-organic frameworks. Adv. Mater. **29**, 12 (2017)
36. Dickinson, M.: Animal locomotion: how to walk on water. Nature **424**, 621–622 (2003)
37. Feng, L., Li, S.H., Li, Y.S., Li, H.J., Zhang, L.J., Zhai, J., et al.: Super-hydrophobic surfaces: from natural to artificial. Adv. Mater. **14**, 1857–1860 (2002)
38. Roach, P., Shirtcliffe, N.J., Newton, M.I.: Progess in superhydrophobic surface development. Soft Matter **4**, 224–240 (2008)
39. Arzt, E.: Overview no130: size effects in materials due to microstructural and dimensional constraints: a comparative review. Acta Mater. **46**, 5611–5626 (1998)
40. Gao, H.J., Ji, B.H., Jager, I.L., Arzt, E., Fratzl, P.: Materials become insensitive to flaws at nanoscale: Lessons from nature. Proc. Natl. Acad. Sci. USA **100**, 5597–5600 (2003)
41. Kraft, O., Gruber, P.A., Monig, R., Weygand, D.: Plasticity in confined dimensions. Annu. Rev. Mater. Res. **40**, 293–317 (2010)
42. Greer, J.R., De Hosson, J.T.M.: Plasticity in small-sized metallic systems: intrinsic versus extrinsic size effect. Prog. Mater. Sci. **56**, 654–724 (2011)
43. Ban, Y.X., Mi, C.W.: Analytical solutions of a spherical nanoinhomogeneity under far-field unidirectional loading based on Steigmann-Ogden surface model. Math. Mech. Solids **25**, 1904–1923 (2020)
44. Manoharan, M.P., Lee, H., Rajagopalan, R., Foley, H.C., Haque, M.A.: Elastic properties of 4–6 nm-thick glassy carbon thin films. Nanoscale Res. Lett. **5**, 14–19 (2010)
45. Lee, C., Wei, X.D., Kysar, J.W., Hone, J.: Measurement of the elastic properties and intrinsic strength of monolayer graphene. Science **321**, 385–388 (2008)
46. Mathur, A., Erlebacher, J.: Size dependence of effective Young's modulus of nanoporous gold. Appl. Phys. Lett. **90**, 061910 (2007)
47. Liu, J.L., Mei, Y., Xia, R., Zhu, W.L.: Large displacement of a static bending nanowire with surface effects. Phys. E **44**, 2050–2055 (2012)
48. Biener, J., Hodge, A.M., Hamza, A.V., Hsiung, L.M., Satcher, J.H.: Nanoporous Au: a high yield strength material. J. Appl. Phys. **97**, 024301 (2005)
49. Biener, J., Hodge, A.M., Hayes, J.R., Volkert, C.A., Zepeda-Ruiz, L.A., Hamza, A.V., et al.: Size effects on the mechanical behavior of nanoporous Au. Nano Lett. **6**, 2379–2382 (2006)
50. Khorshidvand, A.R., Joubaneh, E.F., Jabbari, M., Eslami, M.R.: Buckling analysis of a porous circular plate with piezoelectric sensor-actuator layers under uniform radial compression. Acta Mech. **225**, 179–193 (2014)
51. Huth, M., Kolb, F., Plank, H.: Dielectric sensing by charging energy modulation in a nano-granular metal. Appl. Phys. A Mater. **117**, 1689–1696 (2014)
52. Mojahedin, A., Joubaneh, E.F., Jabbari, M.: Thermal and mechanical stability of a circular porous plate with piezoelectric actuators. Acta Mech. **225**, 3437–3452 (2014)
53. Zhao, Q.S., Papadopoulos, P.: Continuum modeling and simulation of multiphase diffusion through a porous solid. Math. Mech. Solids **20**, 251–267 (2015)
54. Gurtin, M.E., Murdoch, A.I.: Continuum theory of elastic-material surfaces. Arch. Ration Mech. An **57**, 291–323 (1975)
55. Gurtin, M.E., Weissmuller, J., Larche, F.: A general theory of curved deformable interfaces in solids at equilibrium. Philos. Mag. A **78**, 1093–1109 (1998)
56. Sun, K., Shi, J., Ma, L.: Atomistic insights into the effects of residual stress during nanoindentation. Curr. Comput.-Aided Drug Des. **7**, 240 (2017)
57. Shenoy, V.B.: Atomistic calculations of elastic properties of metallic fcc crystal surfaces. Phys. Rev. B **71**, 094104 (2005)
58. Gupta, R., Rai, B.: Effect of size and surface charge of gold nanoparticles on their skin permeability: a molecular dynamics study. Sci. Rep. UK **7**, 45292 (2017)
59. Surblys, D., Kawagoe, Y., Shibahara, M., Ohara, T.: Molecular dynamics investigation of surface roughness scale effect on interfacial thermal conductance at solid-liquid interfaces. J. Chem. Phys. **150**, 114705 (2019)
60. Chen, C.Q., Shi, Y., Zhang, Y.S., Zhu, J., Yan, Y.J.: Size dependence of Young's modulus in ZnO nanowires. Phys. Rev. Lett. 96 (2006)
61. He, J., Lilley, C.M.: Surface effect on the elastic behavior of static bending nanowires. Nano Lett. **8**, 1798–1802 (2008)
62. Wang, Z.Q., Zhao, Y.P., Huang, Z.P.: The effects of surface tension on the elastic properties of nano structures. Int. J. Eng. Sci. **48**, 140–150 (2010)
63. Feng, X.Q., Xia, R., Li, X., Li, B.: Surface effects on the elastic modulus of nanoporous materials. Appl. Phys. Lett. **94**, 011916 (2009)
64. Fang, Q.H., Zhao, L., Li, J.: Surface effects on the elastic modulus of regular polygonal prism nanoporous materials. Acta Mech. **231**, 3451–3460 (2020)
65. Xia, R., Li, X.D., Qin, Q.H., Liu, J.L., Feng, X.Q.: Surface effects on the mechanical properties of nanoporous materials. Nanotechnology **22**, 265714 (2011)
66. Chen, Y., Liu, Y., Fang, Q., Li, J., Liu, Y., Liaw, P.K.: An unified model for dislocations interacting with complex-shape voids in irradiated metals. Int. J. Mech. Sci. **185**, 105689 (2020)

67. Zhang, C., Lu, C., Michal, G., Li, J., Wang, R.: Strong strain hardening in graphene/nanotwinned metal composites revealed by molecular dynamics simulations. Int. J. Mech. Sci. **2021**, 106460 (2021)
68. Zhang, R., Wen, L.H., Xiao, J.Y., Qian, D.: An efficient solution algorithm for space-time finite element method. Comput. Mech. **63**, 455–470 (2019)
69. Niu, R.P., Liu, G.R., Yue, J.H.: Development of a software package of smoothed finite element method (S-FEM) for solid mechanics problems. Int. J. Comp. Meth-Sing. **17**, 1845004 (2020)
70. Boso, D.P., Braga, T., Ravasini, S., Skrbic, T., Puglisi, A., Pinato, O., et al.: An integrated DEM–FEM approach to study breakage in packing of glass cartridges on a conveyor belt. Granul. Matter. **22**, 73 (2020)
71. Vabishchevich, M.O., Solodei, I.I., Chepurnaya, E.A.: Determining the parameters of linear fracture mechanics in dynamic problems based on semianalytical finite-element method. Int. Appl. Mech. **54**, 653–659 (2018)
72. Mi, C.: Surface mechanics induced stress disturbances in an elastic half-space subjected to tangential surface loads. Eur. J. Mech. A Solids **65**, 59–69 (2017)
73. Mi, C.: Elastic behavior of a half-space with a Steigmann-Ogden boundary under nanoscale frictionless patch loads. Int. J. Eng. Sci. **129**, 129–144 (2018)
74. Tian, L., Rajapakse, R.K.N.D.: Finite element modelling of nanoscale inhomogeneities in an elastic matrix. Comput. Mater. Sci. **41**, 44–53 (2007)
75. He, J., Park, H.S.: A methodology for modeling surface effects on stiff and soft solids. Comput. Mech. **61**, 687–697 (2018)
76. Zheng, X.P., Cao, Y.P., Li, B., Feng, X.Q., Wang, G.F.: Surface effects in various bending-based test methods for measuring the elastic property of nanowires. Nanotechnology **21**, 205702 (2010)
77. Goudarzi, T., Avazmohammadi, R., Naghdabadi, R.: Surface energy effects on the yield strength of nanoporous materials containing nanoscale cylindrical voids. Mech. Mater. **42**, 852–862 (2010)
78. Moshtaghin, A.F., Naghdabadi, R., Asghari, M.: Effects of surface residual stress and surface elasticity on the overall yield surfaces of nanoporous materials with cylindrical nanovoids. Mech. Mater. **51**, 74–87 (2012)
79. Kim, G.T., Waizmann, U., Roth, S.: Simple efficient coordinate markers for investigating synthetic nanofibers. Appl. Phys. Lett. **79**, 3497–3499 (2001)
80. Baron, T., Gordon, M., Dhalluin, F., Ternon, C., Ferret, P., Gentile, P.: Si nanowire growth and characterization using a microelectronics-compatible catalyst: PtSi. Appl. Phys. Lett. **89**, 233111 (2006)
81. Sadeghian, H., Yang, C.K., Goosen, J.F.L., van der Drift, E., Bossche, A., French, P.J., et al.: Characterizing size-dependent effective elastic modulus of silicon nanocantilevers using electrostatic pull-in instability. Appl. Phys. Lett. **94**, 221903 (2009)
82. Qiao, L., Zheng, X.J.: Effect of surface stress on the stiffness of micro/nanocantilevers: nanowire elastic modulus measured by nano-scale tensile and vibrational techniques. J. Appl. Phys. **113**, 013508 (2013)
83. Fan, T., Yang, L.H.: Effective Young's modulus of nanoporous materials with cuboid unit cells. Acta Mech. **228**, 21–29 (2017)
84. Lu, Z.X., Xie, F., Liu, Q., Yang, Z.Y.: Surface effects on mechanical behavior of elastic nanoporous materials under high strain. Appl. Math. Mech. Engl. **36**, 927–938 (2015)
85. Antonopoulos, D.C., Dougalis, V.A.: Galerkin-finite element methods for the shallow water equations with characteristic boundary conditions. Ima. J. Numer. Anal. **37**, 266–295 (2017)
86. Singh, S.J., Harsha, S.P.: Thermo-mechanical analysis of porous sandwich S-FGM plate for different boundary conditions using Galerkin Vlasov's method: a semi-analytical approach. Thin Wall Struct. **150**, 106668 (2020)
87. Cuenot, S., Fretigny, C., Demoustier-Champagne, S., Nysten, B.: Surface tension effect on the mechanical properties of nanomaterials measured by atomic force microscopy. Phys. Rev. B 69 (2004)
88. Li, X.X., Ono, T., Wang, Y.L., Esashi, M.: Ultrathin single-crystalline-silicon cantilever resonators: fabrication technology and significant specimen size effect on Young's modulus. Appl. Phys. Lett. **83**, 3081–3083 (2003)
89. Nam, C.Y., Jaroenapibal, P., Tham, D., Luzzi, D.E., Evoy, S., Fischer, J.E.: Diameter-dependent electromechanical properties of GaN nanowires. Nano Lett. **6**, 153–158 (2006)
90. Jing, G.Y., Duan, H.L., Sun, X.M., Zhang, Z.S., Xu, J., Li, Y.D., et al.: Surface effects on elastic properties of silver nanowires: contact atomic-force microscopy. Phys. Rev. B 73 (2006)